HAL
open science

Radar sounding of temperate permafrost in Alaska: Analogy to the Martian midlatitude to high-latitude ice-rich terrains

Joséphine Boisson, Essam Heggy, Stephen Clifford, Kenji Yoshikawa, André Anglade, Philippe Lognonné

To cite this version:

Joséphine Boisson, Essam Heggy, Stephen Clifford, Kenji Yoshikawa, André Anglade, et al.. Radar sounding of temperate permafrost in Alaska: Analogy to the Martian midlatitude to high-latitude ice-rich terrains. Journal of Geophysical Research, 2011, 116 (E11), 10.1029/2010JE003768 . insu-02564101

HAL Id: insu-02564101

https://insu.hal.science/insu-02564101

Submitted on 27 May 2020

HAL is a multi-disciplinary open access archive for the deposit and dissemination of scientific research documents, whether they are published or not. The documents may come from teaching and research institutions in France or abroad, or from public or private research centers.

L'archive ouverte pluridisciplinaire **HAL**, est destinée au dépôt et à la diffusion de documents scientifiques de niveau recherche, publiés ou non, émanant des établissements d'enseignement et de recherche français ou étrangers, des laboratoires publics ou privés.

Radar sounding of temperate permafrost in Alaska: Analogy to the Martian midlatitude to high-latitude ice-rich terrains

Joséphine Boisson,[1] Essam Heggy,[2] Stephen M. Clifford,[3] Kenji Yoshikawa,[4] André Anglade,[1] and Philippe Lognonné[1]

Received 29 October 2010; revised 24 August 2011; accepted 25 August 2011; published 16 November 2011.

[1] Radar detection of subsurface ice on Mars has been widely debated in part because the dielectric signature of ice, as deduced from the dielectric constant, can be confused with dry-silicate-rich materials. To identify the ice dielectric signature, it is crucial to estimate the imaginary part of the dielectric permittivity inferred from the dielectric attenuation after removing the scattering loss. Unfortunately, the latter remains poorly quantified at both Mars Advanced Radar for Subsurface and Ionospheric Sounding (MARSIS) and shallow subsurface radar SHARAD frequencies. To address this ambiguity, we conducted multiple-frequency ground-penetrating radar and resistivity investigations in well-characterized temperate permafrost in Fairbanks, Alaska. The area shows several geomorphologic similarities to midlatitude and high-latitude terrains on Mars. This approach allowed us to quantify the dielectric and scattering losses in temperate permafrost over the 10 to 1000 MHz frequency band. At 20 MHz, our results suggest an average dielectric loss rate of 0.25 ± 0.03 dB/m, whereas the corresponding average scattering loss rate is 0.94 ± 0.37 dB/m. The scattering loss was found to represent ~69% of the total signal attenuation. Considering this result and the study by Heggy et al. (2006a) in volcanic environments, we revised the interpretation of the attenuation coefficient calculated from SHARAD data over the Deuteronilus Mensae region and Amazonis Planitia; we then used the reevaluated dielectric loss to estimate the imaginary part of the dielectric permittivity. Our results suggest that even if Deuteronilus Mensae deposits and the Vastitas Borealis Formation may have similar dielectric constants, their imaginary parts are different. This implies that the two regions have different bulk compositions, with the former being ice-rich sediments and the latter being nonconsolidated volcanic deposits.

Citation: Boisson, J., E. Heggy, S. M. Clifford, K. Yoshikawa, A. Anglade, and P. Lognonné (2011), Radar sounding of temperate permafrost in Alaska: Analogy to the Martian midlatitude to high-latitude ice-rich terrains, *J. Geophys. Res.*, *116*, E11003, doi:10.1029/2010JE003768.

1. Introduction

[2] Subsurface water on Mars has been the subject of numerous hypotheses and debates [*Kuzmin*, 1983; *Fanale et al.*, 1986; *Clifford*, 1993; *Mellon and Jakosky*, 1993, 1995; *Clifford and Parker*, 2001; *Grimm and Painter*, 2009; *Clifford et al.*, 2010], because it has important implications for the hydrological and climatic evolution of the planet. Thus, the study of the actual distribution and state of subsurface water is one of the high-priority goals of the Mars Exploration Program [*Clifford*, 1993]. In this paper, we discuss permafrost detection with subsurface radar.

[3] Radar waves are sensitive to variations in the electrical properties of rocks and to the presence of water (as a liquid or solid), whether on the surface or in the subsurface. For these reasons, radar sounders offer among the most promising geophysical techniques to investigate the distribution of subsurface water. Two low-frequency sounding radars are currently probing the Martian upper crust, exploring potential evidence of subsurface water. The Mars Advanced Radar for Subsurface and Ionospheric Sounding (MARSIS), on board the European Space Agency's (ESA's) 2003 Mars Express spacecraft, operates at four 1 MHz wide frequency bands between 1.8 and 5 MHz [*Picardi et al.*, 2004]. Additional low-frequency radar investigations have been conducted by the shallow subsurface radar (SHARAD) on board NASA's 2005 Mars Reconnaissance Orbiter spacecraft; SHARAD probes the subsurface using a single 10-MHz-wide band, centered at 20 MHz [*Seu et al.*, 2004]. SHARAD's higher frequency yields a better vertical resolution than MARSIS (~10–20 m compared with ~50–100 m for MARSIS), but its maximum sounding depth is shallower. In 2018, these

[1]Institut de Physique du Globe de Paris et Université Paris Diderot, Sorbonne Paris Cité, UMR CNRS 7154, Saint Maur des Fossés, France.
[2]Jet Propulsion Laboratory, Pasadena, California, USA.
[3]Lunar and Planetary Institute, Houston, Texas, USA.
[4]Water and Environmental Research Center, University of Alaska Fairbanks, Fairbanks, Alaska, USA.

Copyright 2011 by the American Geophysical Union.
0148-0227/11/2010JE003768

orbital sounding investigations will be followed by another, higher-frequency investigation of the planet's surface by a ground-penetrating radar (GPR) mounted on ESA's ExoMars rover. The Water Ice and Subsurface Deposit Observations on Mars (WISDOM) instrument is designed to operate over a much broader and higher-frequency range (0.5–3 GHz) to investigate the properties of the Martian shallow subsurface (top ~1–3 m) and provide information about potential targets for the rover's onboard drill [*Ciarletti et al.*, 2009].

[4] Analysis of several years' worth of radar sounding data, acquired by MARSIS and SHARAD, has resulted in the identification of a number of potentially ice-rich terrains at low latitudes to midlatitudes. For example, *Watters et al.* [2007] analyzed the MARSIS data obtained over the Medusae Fossae formation (MFF; ~130°E–240°E, ~10°S–10° N) and found that these deposits have a surprisingly low mean bulk real dielectric constant, ~2.9 ± 0.4, consistent with either an ice-rich material or volcanic ash deposit. This result has been confirmed by a similar analysis of SHARAD observations over this same area [*Carter et al.*, 2009]. Putative large ice-rich masses have also been detected by SHARAD over the Deuteronilus Mensae area (40°N–51°N, 14°E–35°E), associated with lobate debris aprons (LDAs) [*Plaut et al.*, 2009]. Those recent results are important for climate evolution study but remain ambiguous. Indeed, radar detection of Martian subsurface ice is not trivial and remains poorly constrained.

[5] The ice dielectric signature, as expressed by the dielectric permittivity's real part (~3.15–3.18), cannot be distinguished from that of porous low-loss silicate materials such as volcanic ash or loose, dry sediments. Therefore, analysis of Martian radar sounder data needs to take into account the dielectric permittivity's imaginary part to uniquely identify subsurface ice signature. Moreover, Martian radar sounder data analyses do not consider scattering phenomenon, which depends on the degree of heterogeneity of the sounded subsurface and accounts for a part of the total calculated radar signal loss. Hence, the identification of subsurface ice in the GPR data is constrained by our understanding of the dielectric and scattering losses arising from the dielectric complexity and structural heterogeneity of the Martian subsurface.

[6] To better constrain those results, analog terrains need to be investigated to well characterize the radar signal behavior on an ice-rich environment. Although some GPR surveys have investigated these properties in Mars-analog volcanic terrains [*Paillou et al.*, 2001; *Grant et al.*, 2004; *Grimm et al.*, 2006; *Heggy et al.*, 2006a, 2006b] and permafrost terrains [*Arcone et al.*, 2002; *Leuschen et al.*, 2003; *Yoshikawa et al.*, 2006], the complexity of the different loss mechanisms remains poorly constrained.

[7] To address this deficiency, we conducted multifrequency GPR and resistivity investigations in an analog of Mars permafrost terrain, located ~21 km north of Fairbanks, Alaska (central interior region of Alaska; Figure 1a; the analogy is discussed in section 2.2). Beyond the presence of frozen ground, the area also possesses several geomorphological similarities to some regions of Mars, including patterned ground [*Boike and Yoshikawa*, 2003] and pingos [*Yoshikawa et al.*, 2006]. The surveys were performed in an area known as Vault Creek (north of Fairbanks; Figure 1b). The site includes a 200 m long mine (Figure 1c) that reaches a maximum depth of 40 m and provides an opportunity to visualize the differences in subsurface lithology, composition, stratigraphy, and structural heterogeneity. We used four different antennas (at central frequencies of 40, 270, 400, and 900 MHz) to collect data along the same profile, allowing us to study the frequency dependence of the attenuation mechanisms over a wide frequency band. The resulting data have helped characterize and quantify the different frequency-dependent loss mechanisms (mainly scattering and dielectric attenuations) that affect the propagation of radar signals in temperate permafrost. We conducted this study and we used other analog investigations [*Grimm et al.*, 2006; *Heggy et al.*, 2006a] to allow us to remove estimated scattering loss from the measured Martian radar signal loss. Subsequently, we can obtain a revised dielectric attenuation coefficient and infer the imaginary part of the dielectric constant. This, in turn, should assist in understanding and constraining the ambiguities associated with the low-frequency GPR identification and mapping of subsurface ice in the Martian midlatitudes.

2. Site Description and Analogy

2.1. Geology of the Vault Creek Site

[8] The Fairbanks area is in the discontinuous permafrost zone, which means that 50% to 90% of the subsurface is frozen. It is located in the central interior of Alaska, approximately 420 km north of Anchorage (Figure 1a). This region has a subarctic climate that, in some areas, permits the survival of temperate permafrost (ground temperature between −1°C and 0°C) throughout the year, beneath an active layer that is ~0.5–1 m deep (i.e., the depth to which the near-subsurface undergoes seasonal freeze or thaw) [*Arcone and Delaney*, 2003; *Marchenko et al.*, 2008]. In the Vault Creek area (the site investigated in this study), the permafrost extends to a depth of ~120 m (this depth is from borehole U63 from the Global Terrestrial Network for Permafrost), below which the local geothermal gradient results in subsurface temperatures that rise above freezing. Our GPR and resistivity surveys were conducted during the first two weeks of March 2008, when the ground, including the active layer, was totally frozen.

[9] The field site is along an unvegetated trail above a gold mine located along Vault Creek, close to the mouth of Treasure Creek (Figures 1b and 1c). The Vault Creek valley presents different periglacial landforms, such as collapsed pingos [*Newberry et al.*, 1996] and possible thermokarst depressions filled by water. The mine is a 200 m long tunnel that angles down from the surface and reaches a maximum depth of 40 m, providing opportunities to conduct sounding investigations both over and within the mine. Figure 2 shows an inferred stratigraphic column of the Vault Creek site (obtained from stratigraphy observed inside the tunnel) down to the maximum depth reached by the tunnel. The bedrock is composed of eclogite-bearing schist amphibolites overlain by ~30 m of reworked creek gold-bearing gravel [*Péwé*, 1955; *Sellmann*, 1967]. An ~10 m layer of aeolian and retransported silt overlies the creek gravel layer. The composition and lithology of the different layers discussed

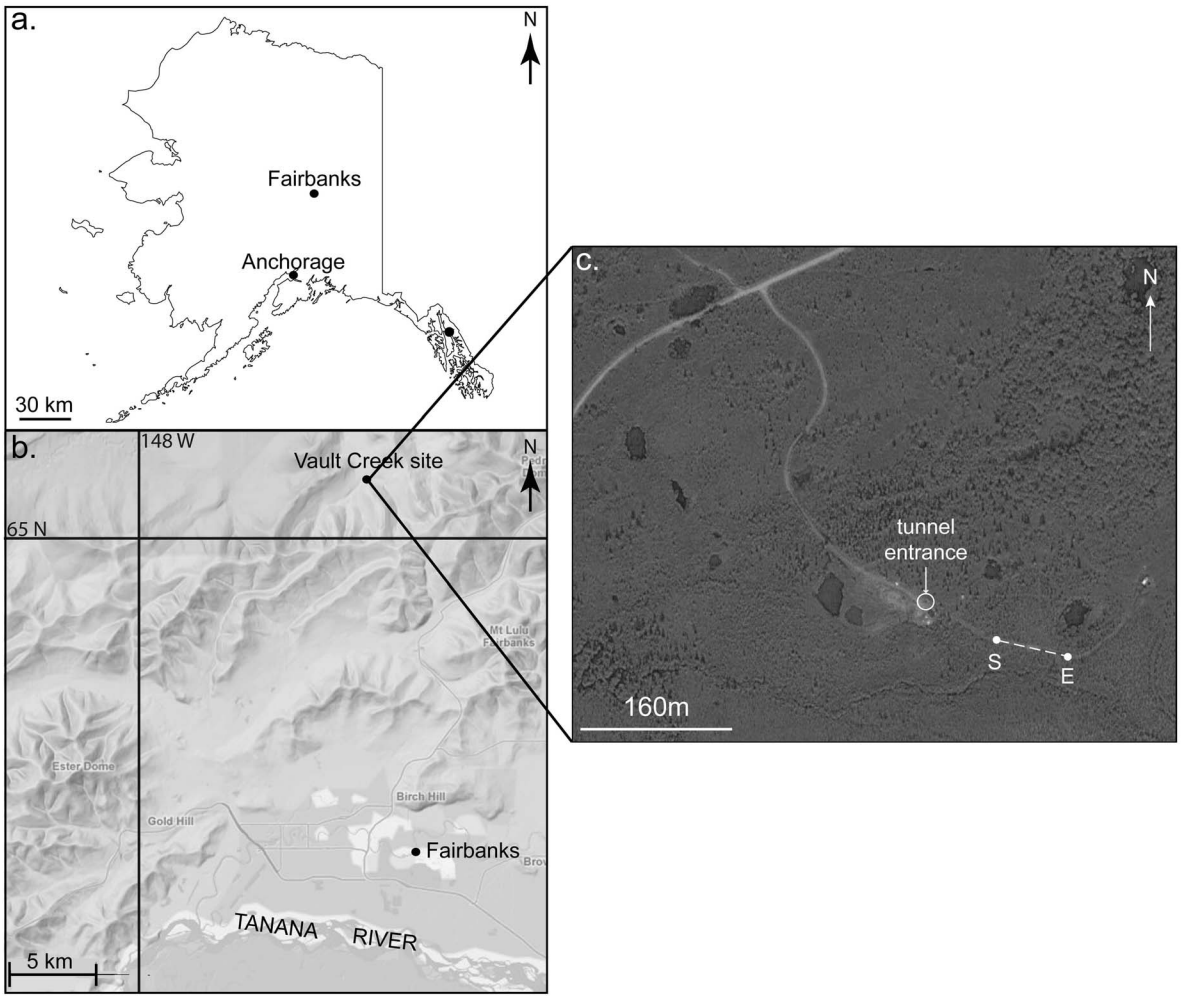

Figure 1. (a) Map of the state of Alaska (© 2007–2011 Daniel Dalet, http://d-maps.com). (b) Enlargement of the Fairbanks area. The geophysical survey was conducted at the Vault Creek site, north of Fairbanks (http://seamless.usgs.gov/). (c) 5 m orbital visible image of the Vault Creek site. Google Earth imagery © Google Inc. and DigitalGlobe, Inc. Used with permission.

below are based on different studies performed in the Cold Regions Research and Engineering Laboratory (CRREL) permafrost tunnel, located 9 km southeast of our tunnel.

[10] The Fairbanks silt layer consists of 50%–70% silica by weight and of 15%–20% potassium feldspar (e.g., orthoclase) [*Péwé*, 1955; *Arcone et al.*, 2008]. A recent detailed study of the Fairbanks silt mineralogy [*Arcone et al.*, 2008] indicates that it is composed of 17% clays (kaolonite, illite, and montmorillonite). This value is greater than the one in the study by *Newberry et al.* [1996], which suggests a clay content lower than 10%. The presence of clays increases the total Fairbanks silt-specific surface area (54.7 $m^2\ g^{-1}$ [*Arcone et al.*, 2008]) and thus increases the adsorbed water (also often referred to as unfrozen water) content. The silt contains a large-volume fraction of ground ice. A precise geologic study realized in the CRREL permafrost tunnel indicated 54%–79% by volume of ice in the Fairbanks silt [*Sellmann*, 1967]. The amount of ice in the silts of the Vault Creek tunnel is likely similar because the mean temperatures of the permafrost are close (−0.6°C and −0.7°C). The ice is in three forms: (1) small lenses, millimeters to centimeters thick and meters wide, (2) massive ice wedges up to a few meters in scale (in the Vault Creek site tunnel, we observed those cryostructures also in the gravel layer), and (3) disseminated ice. Thus, even if the silt presents a homogeneous grain size distribution (from a few micrometers to 100 μm) [*Péwé*, 1955; *Arcone et al.*, 2008], the presence of ice wedges and lenses in this layer introduces an important heterogeneity at different scales. Moreover, adsorbed water migrates toward ice wedges and lenses in the Fairbanks silt layer. The Fairbanks silt sampled in the CRREL tunnel contains ~1.5%–7.5% organic matter [*Sellmann*, 1967]. As Fairbanks silt is the same geological entity [*Newberry et al.*, 1996] in the CRREL tunnel and at the Vault Creek site, we assume that Vault Creek has the same amount of organic matter. This organic material introduces dielectric heterogeneities inside the silt layer and generates scattering on the GPR signal at the high-frequency bands. Moreover, the Vault Creek site is covered by vegetation. Nevertheless, the surveys were performed along an unvegetated trail to avoid any clutter on

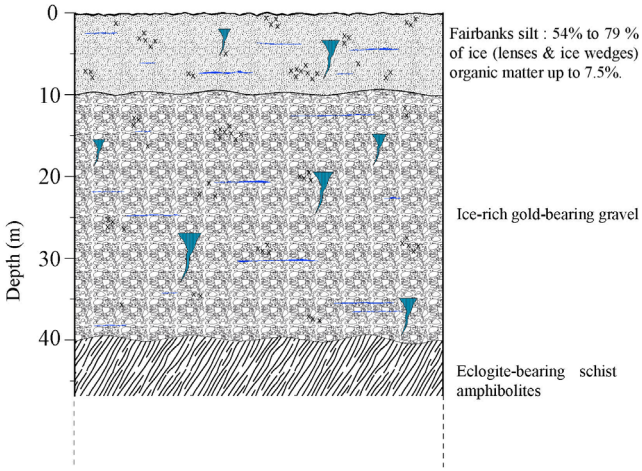

Figure 2. Lithologic cross sections of the subsurface at the Vault Creek site subsurface observed in the 40m deep tunnel. The ice-rich Fairbanks silt is composed of 17% clay minerals [*Arcone et al.*, 2008] and 1.5%–7.5% organic matter [*Sellmann*, 1967]. Ice in the Fairbanks silt and gravel layers is in the form of polarimetric ice wedges and centimeter-thick segregation lenses, as shown by symbols represented in the different layers of the cross section.

the signal, which can be generated by a layer of organic material. All but the top ~0.5–1.5 m of this stratigraphy is perennially frozen.

2.2. Analogy of the Fairbanks Area to Martian Permafrost

[11] Various studies have highlighted the geomorphologic similarities between some landforms and surface features present on Mars and those found in ice-rich permafrost and periglacial environments on Earth; these features include patterned ground, pingo-like features, LDAs, and evidence suggestive of the interaction between volcanism and ground ice [*Carr and Schaber*, 1977; *Rossbacher and Judson*, 1981; *Lucchitta*, 1981, 1985; *Mouginis-Mark*, 1985; *Squyres and Carr*, 1986; *Carr*, 1986, 1996; *Squyres et al.*, 1992; *Hiesinger and Head*, 2000; *Head et al.*, 2003; *Mangold et al.*, 2004; *Costard et al.*, 2007]. For this reason, studies of terrestrial permafrost and periglacial environments are of great interest for understanding the potential physical and electromagnetic properties of water and ice in the Martian subsurface [*Farr et al.*, 2001; *Farr*, 2004]. Alaska hosts a wide variety of permafrost and periglacial landforms (e.g., glaciers, ice wedges and lenses, polygonal terrains, thermokarst, and pingos), which has led to its recognition as one of the terrestrial periglacial analogs of Mars [*Kargel et al.*, 1993; *Farr et al.*, 2001; *Farr*, 2004; *Arcone et al.*, 2002]. The area around Fairbanks, Alaska, offers a case study of such terrains, which are readily accessible with minimum logistical concerns.

[12] While the geomorphic similarities between Martian cold-climate features and their terrestrial counterparts are readily apparent, the similarity between their physical and geophysical characteristics is less clear. Indeed, the range of mean annual temperatures on Mars, from a high of ~218 K at the equator to as little as 150 K at the poles, could potentially result in a lower volumetric content of adsorbed water and consequently less radar attenuation by conduction and dielectric relaxation. However, empirical studies have demonstrated that such films remain unfrozen on mineral surfaces down to temperatures lower than the freezing point, 273 K [*Anderson et al.*, 1967; *Anderson and Tice*, 1973], particularly in the presence of potent freezing-point-depressing salts [*Banin and Anderson*, 1974]. Indeed, compositional studies of the Martian regolith suggest that it is salt rich, including freezing-point depressors such as sodium chloride, calcium chloride, and magnesium perchlorate [*Brass*, 1980; *Clark and Van Hart*, 1981; *Burt and Knauth*, 2002; *Fairén et al.*, 2009; *Hecht et al.*, 2009], which have freezing points at their eutectics of 252, 218, and 203 K, respectively. Thus, salts in the Martian subsurface could result in the presence of adsorbed water even at the low Martian surface temperature [*Pommerol et al.*, 2009; *Stillman et al.*, 2010]. Moreover, on Mars, the diffusion of water vapor across the regolith [*Clifford et al.*, 2010] may produce adsorbed films of water around the soil particles, especially if the soil is salt rich [*Zent*, 2008]. This hypothesis has been confirmed by a quantitative study on Martian regolith analogs [*Pommerol et al.*, 2009].

[13] For a specific surface area of ~17 m^2 g^{-1} for the Martian regolith, as determined by *Ballou et al.* [1978] from the Viking 1 landing site physical properties (indicative of clays in the Viking 1 soil composition in Chryse Planitia at 22.48°N, 47.97°W), ice-rich permafrost on Mars would contain an appreciable volumetric content of adsorbed water, similar to that of terrestrial temperate permafrost. As mentioned in section 2.1, the Fairbanks silt is 17% clays [*Arcone et al.*, 2008], which are mainly kaolinite, montmorillonite, and illite. Those phyllosilicates have also been detected at different places in the Martian regolith [*Poulet et al.*, 2005; *Bibring et al.*, 2006; *Mustard et al.*, 2008].

[14] Ice wedges that can be observed in the subsurface of the Vault Creek investigation site (see section 2.1) have also been directly and indirectly observed on Mars. Indeed, ice wedges are residues of polygonal fractures filled by ice, and much polygonal ground has been observed on Mars [*Mutch et al.*, 1976; *Lucchitta*, 1981; *Head et al.*, 2003; *Yoshikawa*, 2003; *Mangold*, 2005; *Smith et al.*, 2007; *Mellon et al.*, 2008; *Levy et al.*, 2009].

[15] In section 6, we consider the implication of our result on the Martian radar data analysis, especially on the SHARAD data analysis over the LDAs in the Deuteronilus Mensae area [*Plaut et al.*, 2009]. The validity and limitation of the analogy between the Vault Creek site and the Martian area of Deuteronilus Mensae are discussed below. Deuteronilus Mensae (centered on 40°N and 20°E) is located in the range of latitude (35°–50°) where ground ice is hypothesized to be stable at a few meters deep [*Squyres and Carr*, 1986]. This hypothesis is supported by radar sounding observations [*Plaut et al.*, 2009] and by observation of several morphologies associated with ice-rich subsurfaces [*Squyres*, 1978; *Mangold*, 2003]. Indeed, the formation of LDAs and fretted terrains observed by the Viking cameras, Mars Orbiter Camera, and recently the High Resolution Imaging Science Experiment (HiRISE) have been suggested to be driven by the sublimation of ground ice (guided by heterogeneities like subsurface fractures) [*Squyres*, 1978, 1979; *Mangold*, 2003; *Head et al.*, 2006]. The amount of ice

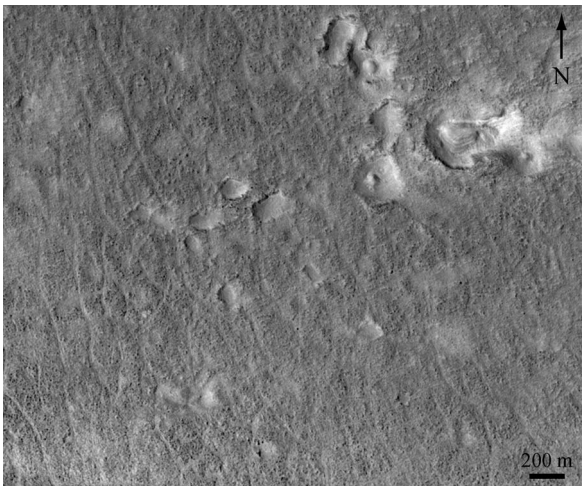

Figure 3. Polygon terrain observed in Deuteronilus Mensae. Detail of HiRISE image ESP_015944_2225 (resolution: 25 cm/pixel) centered on 42.2°N and 18.4°E (Courtesy: NASA/JPL/Caltech and the University of Arizona). The location of this terrain corresponds to the location of Figure 2 [*Plaut et al.*, 2009].

in the LDAs needs to be higher than ~30% to explain the deformation observed in this area [*Mangold et al.*, 2002]. Thus, the value could be comparable to one of the Fairbanks silts (~50%–70%) but the exact amount of ice in LDAs is still controversial [*Plaut et al.*, 2009]. *Bibring et al.* [2006] suggested the occurrence of phyllosilicates in the Deuteronilus Mensae area. Similar to Fairbanks silts, the presence of phyllosilicates increases the surface-specific area of the Deuteronilus Mensae subsurface and consequently increases the amount of adsorbed water that can be stored in the LDAs. This amount could be increased by the presence of salt in the subsurface [*Stillman and Grimm*, 2011], even at the Martian low temperature (~210 K at Deuteronilus Mensae latitudes) [*Mellon and Jakosky*, 1993]. Thus, we can reasonably hypothesize that the Deuteronilus Mensae subsurface may generate radar signal dielectric attenuation because of the presence of adsorbed water in a fashion similar to the Fairbanks silts.

[16] Other landforms related to an ice-rich subsurface can be observed on the Vault Creek site, such as collapsed pingo [*Newberry et al.*, 1996] and possible thermokarst formations. Those features have been widely observed and studied on Mars [*Costard and Kargel*, 1995; *Soare et al.*, 2007; *Burr et al.*, 2009; *Lefort et al.*, 2010; *Séjourné et al.*, 2011]. HiRISE images revealed the presence of pingos [*Dundas and McEwen*, 2010] and polygon terrains (Figure 3) in Deuteronilus Mensae. Thus, the Deuteronilus Mensae subsurface is certainly composed of ice heterogeneities like the ice wedges on the Vault Creek subsurface. The heterogeneity degree of the Deuteronilus subsurface is also important because the ground is intensely fractured. [*Mangold*, 2003].

[17] The above discussion suggests that even if the analogy is not perfect (different ice content, different composition), the Vault Creek site has a substantial geomorphological and geophysical analogy to the Martian midlatitude terrain of Deuteronilus Mensae. Hence, terrestrial cold-climate environments are better analogs of Mars than temperature considerations alone might suggest.

3. Survey Setup

[18] The GPR and resistivity investigations were performed in March 2008, along a trail located above the Vault Creek gold mine tunnel to allow correlation between the radar's loss signal and the ground resistivity.

3.1. Resistivity Survey

[19] A two-dimensional resistivity electrical resistivity tomography (ERT) profile was performed using the SYSCAL Pro Switch system manufactured by IRIS Instruments, Orléans, France. In the ERT method, an electric current (I) is injected and received between the outer electrodes, and a potential difference (V) is measured between the inner electrodes [*Yoshikawa et al.*, 2006]. Then, an apparent resistivity ρ_a is calculated from

$$\rho_a = 2\pi a V / I, \tag{1}$$

where a is the distance between the electrodes. For the acquisition along the radar traverse, we deployed 24 electrodes, spaced at 5 m intervals. We selected the Wenner electrode configuration for its accurate horizontal resolution [*Reynolds*, 1997]. For the Wenner measurement protocol, the SYSCAL Pro Switch unit automatically selects the injection and measurement electrodes sequence. The minimum electrode spacing was set initially at 5 m and increased progressively to measure more deeply. Each measurement was repeated over six acquisition cycles to obtain a standard deviation (measurement quality factor) lower than 1% of the measured value. The processing and analysis of the field-acquired data are detailed in section 5.1.

3.2. GPR Sounding

[20] The GPR surveys were conducted using the commercial SIR-3000 system manufactured by Geophysical Survey Systems, Inc. (GSSI), Salem, New Hampshire. In order to understand the frequency dependence of dielectric and scattering losses over a frequency range wide enough to cover current and future radar subsurface probing experiments, we used four different radar sounding antennas with manufacturer-designated pulse center frequencies of 40, 270, 400, and 900 MHz (of which only the 40 MHz is an unshielded antenna). When the bandwidths of the above-cited antennas are combined, they provide continuous radar subsurface backscatter echo measurements from 30 to 1100 MHz. During the acquisition, the antennas had optimized contact with the ground to reduce surface coupling loss. The 270, 400, and 900 MHz antennas were closely placed in a single unit and were virtually in a monostatic mode, whereas the 40 MHz antennas were more widely separated (1.9 m) in a bistatic mode. For the 40 MHz antenna profile, the data were acquired in point mode at 1 m intervals; whereas the 270, 400, and 900 MHz profiles used a continuous mode and acquired a single radar trace per centimeter. For the four GPR surveys, data were acquired with the same time range sampling of 1024 (16 bits). The sounding echo range was set to 1000 ns (with a time

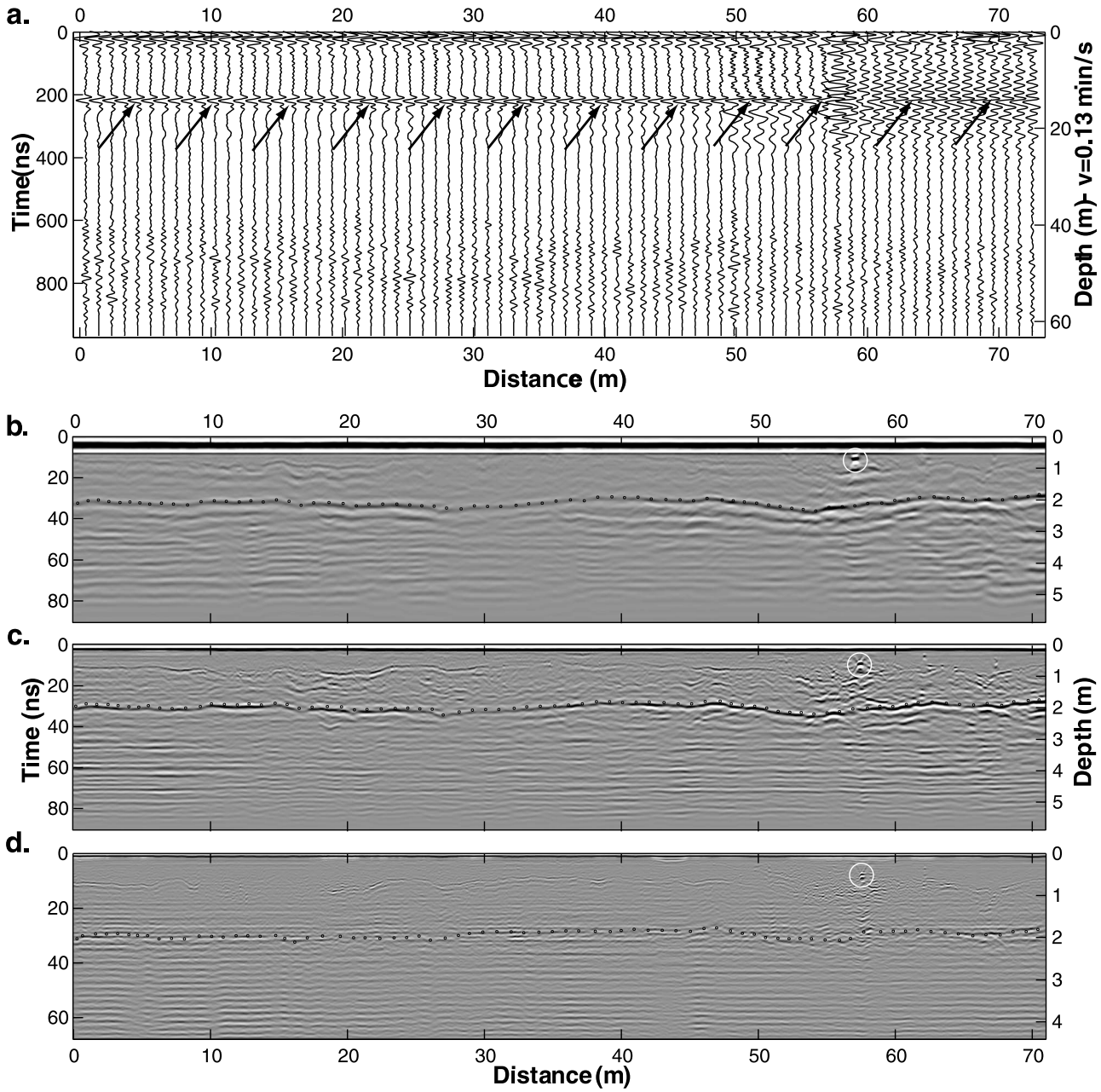

Figure 4. (a) Radargram of the 40-MHz antenna survey. As it was acquired in point mode at 1 m intervals, the radargram is displayed with individual traces. The black arrows highlight a reflection that is due to any features in the time range of 200 ns. (b) 270 MHz, (c) 400 MHz, and (d) 900 MHz antenna radargrams (central frequency has been shifted to 180, 300, and 750 MHz, respectively.) The black dotted line highlights an interface where the soil temperatures are $-2°C < T < -1°C$. Open circles show a local diffractor that generated a hyperbola before migration of the data.

increment of 0.98 ns) for the 40 MHz antenna, 100 ns (with a time increment of 0.1 ns) for both the 270 and 400 MHz antennas, and 75 ns (with a time increment of 0.075 ns) for the 900 MHz antenna.

[21] The survey resulted in four 72 m long radargrams corresponding to each of the four central frequencies. The traverse's start point (designated by S in Figure 1c) is located at 65°01.747′N and 147°42.263′W, and the end point (designated by E in Figure 1c) is located at 65°01.737′N and 147°42.164′W. Figure 1c shows the traverse location and the surrounding field conditions.

[22] Data stacking of eight traces was applied during the acquisition to increase the signal-to-noise ratio (SNR). We applied an average-trace-removal filter to the radargrams to eliminate constant coherent noise. Finally, to remove hyperbolas generated by punctual scatterers in the subsurface, the radargrams were migrated. Figure 4a is the resulting 40 MHz antenna profile. It appears with individual traces

because it was acquired in point mode (trace taken each meter), unlike the three other profiles (Figures 4b, 4c, and 4d), which were acquired in a continuous mode. The black arrows (Figure 4a) highlight a reflection at 200 ns after the first arrival. The waveform and the arrival time of this reflection are constant all along the profile. It is hence difficult to attribute this reflection to a geologic structure in the subsurface. However, the unshielded nature of the 40 MHz antenna implies that the reflection could be generated by any feature within a time range of 200 ns around the antenna.

[23] Figures 3b, 3c, and 3d are the radargrams for the 270, 400, and 900 MHz antennas profiles, respectively. These three figures show an interface varying from 1.5 to 1.7 m (black dotted lines, most likely the bottom of the active layer). This interface corresponds to soil temperatures $-2°C < T < -1°C$, where the dielectric constant of the frozen silt increases significantly (see section 4.2) [*Delaney and Arcone*, 1982; *Arcone and Delaney*, 1984; *Delaney and Arcone*, 1984]. The depth of this interface as interpreted from the radargrams agrees with the $-2°C < T < -1°C$ depth (~1.5 m) observed in the temperature-to-depth profile, shown in Figure 5 (see section 4.2). This transition depth is observed more clearly in the 270 and 400 MHz radargrams than in the one obtained at 900 MHz. This is explained by the higher dielectric contrast at lower frequencies and the fact that the depth of this interface is nearly equal to the maximum depth of investigation for the 900 MHz antenna, making the reflected signal barely detectable above the noise. It is important to notice that the central frequency of each emitted signal is shifted to a lower frequency. Indeed, the presence of heterogeneities inside the silts generates scattering and energy losses at a wavelength equal to the heterogeneity size. This phenomenon acts like a low-pass filter on the signal. Thus, the spectrum of the 900 MHz antenna signal is shifted down to ~750 MHz central frequency (it could vary from trace to trace along the profile), and the spectra of the 400 and 270 MHz antennas signal are shifted to 300 and 180 MHz central frequencies, respectively. For the 40 MHz antenna profile, the central frequency of the received signal is approximately the same (~38 MHz) as the frequency of the emitted signal.

[24] The data processing conducted to analyze the frequency dependence of these results is detailed in section 5.2.

4. Assessment of the Different Radar Wave Attenuation Mechanisms

[25] The total signal loss includes attenuation caused by geometric spreading, the intrinsic electromagnetic properties of the medium, and scattering by embedded interfaces and objects. Below we briefly describe each of these mechanisms as they relate to our quantification of both the dielectric and scattering components discussed in section 5.2.

4.1. Geometric Spreading

[26] Geometric spreading results in signal loss caused by the increased area of the expanding wavefront (i.e., energy distributed over a growing sphere). It can be described by the general radar equation [*Stratton*, 1941; *Skolnik*, 1990]

$$\frac{P_R}{P_T} = \frac{G^2\lambda^2\xi}{64\pi^3R^4}e^{-4\alpha R} \tag{2}$$

where P_R is the received power, P_T is the transmitted power, G represents antenna gain, λ is the wavelength of the radar wave in the medium, R is the distance from antenna to target, and α is the intrinsic attenuation coefficient (detailed further in section 4.2). The backscattered cross section ξ depends on the target considered. As mentioned in section 2.1, the Fairbanks silt contains mainly icy heterogeneities. Thus we consider three models of reflecting target. The first is for an infinite smooth planar reflector in which $\xi = \pi R^2 r^2$, where r is the amplitude reflection coefficient [*Annan and Davis*, 1977; *Reynolds*, 1997]. Therefore, the ratio P_R/P_T is proportional to $1/R^2$. We also considered a model in which the GPR echoes are integrated over the diameter of the first Fresnel zone; therefore, $\xi = \pi\lambda R r^2/2$. This model is also used for a rough planar reflector. The ratio P_R/P_T is thus proportional to $1/R^3$ [*Annan and Davis*, 1977; *Reynolds*, 1997]. Finally, we considered a third model of Rayleigh scatterers (subwavelength-scale spheres) for which $\xi = \pi^5 d^6 r^2/\lambda^4$, where d is the radius of the sphere [*Stratton*, 1941; *Annan and Davis*, 1977]. Thus, the ratio P_R/P_T is proportional to $1/R^4$.

[27] As the heterogeneities distribution in the Fairbanks silts below the trail is not known, we assumed that the ice heterogeneities are randomly distributed.

4.2. Dielectric Attenuation

[28] The dielectric loss is associated with the decrease of electric field amplitude during propagation into an attenuating dielectric. The signal decay produced by this dielectric attenuation exhibits an exponential behavior ($e^{-4\alpha R}$; see equation (2)). The dielectric attenuation is commonly represented by the attenuation coefficient α:

$$\alpha = \omega\sqrt{\frac{\mu\varepsilon_e}{2}\left(\sqrt{1+\tan^2\delta}-1\right)}, \tag{3}$$

where ω is the angular frequency, μ ($= \mu' - i\ \mu''$) is the complex magnetic permeability, ε_e ($= \varepsilon_e' - i\ \varepsilon_e''$) is the complex effective permittivity, and $\tan\delta$ is the loss tangent (i.e., the ratio between the imaginary and real parts of the permittivity [*Ulaby et al.*, 1982]). For frozen silts, there is insignificant magnetic permeability; hence $\mu' = 1$ and $\mu'' = 0$. Therefore, equation (3) becomes

$$\alpha = \frac{\omega}{c}\sqrt{\frac{\varepsilon_r'}{2}\left(\sqrt{1+\left(\frac{\varepsilon_r''}{\varepsilon_r'}\right)^2}-1\right)}, \tag{4}$$

where c is the speed of light and ε_r' and ε_r'' are the real and imaginary parts, respectively, of the dielectric constant. The attenuation coefficient α can be expressed in decibels per meter: $\alpha_{dB} = 20\log_{10}(e\alpha) = 8.686\alpha$ [*Grimm et al.*, 2006].

[29] To quantify the dielectric loss, the frequency dependence of the dielectric permittivity for each subsurface material has to be identified. To describe the frozen silt dielectric permittivity, we use the *universal dielectric response model* developed by *Jonscher* [1977] and simplified by *Hollender and Tillard* [1998] for the case of the radar frequencies range:

$$\varepsilon_e(\omega)\varepsilon_0\chi_r\left(\frac{\omega}{\omega_r}\right)^{n-1}\left[1 - i\cot\left(\frac{n\pi}{2}\right)\right] + \varepsilon_\infty, \tag{5}$$

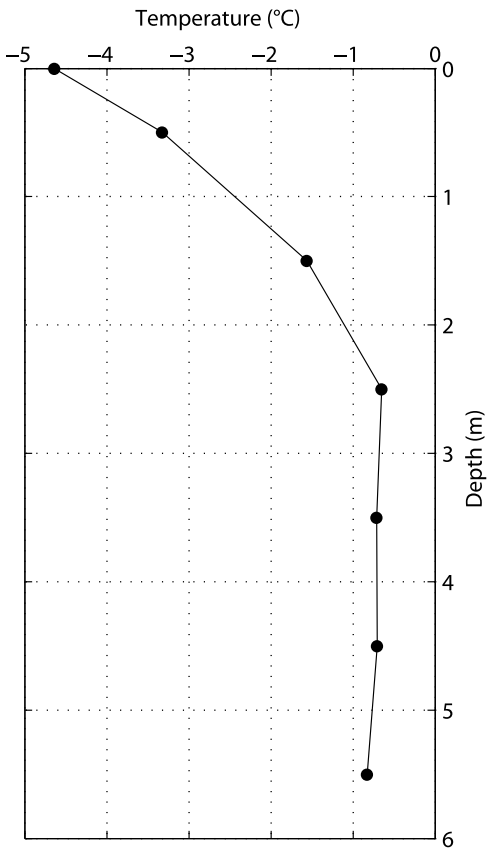

Figure 5. Average temperature (in degrees Celsius) versus depth (in meters) dependency for the Fairbanks frozen silt during March 2008. (K. Yoshikawa, personal communication, 2010).

where ε_0 is the free-space permittivity; χ_r and ω_r are the real part of the electric susceptibility and the angular reference frequency, respectively; n is a coefficient that is between 0 and 1 ($n = 1$ for a low-loss dielectric material); and ε_∞ is the real part of the effective permittivity at a very high frequency. For the Fairbanks silt, ε_∞ is 3.2 [*Arcone*, 1984]. It has to be noticed that at the radar frequencies, for a low-loss medium (e.g., frozen silt at temperatures <−2°C), the Jonscher law can be simplified by neglecting the $\varepsilon\infty$ contribution [*Bano*, 1996].

[30] The Fairbanks silt dielectric permittivity depends on the soil temperature. Indeed, the dielectric permittivity (both real and imaginary parts) increases significantly between −2°C and −1°C from ~7.3 to 11 for the real part at 100 MHz [*Arcone and Delaney*, 1984; *Delaney and Arcone*, 1984; *Arcone and Delaney*, 1989]. This is caused by the large specific surface area of clay minerals included in the Fairbanks silt, which contains adsorbed water that will increase the dielectric permittivity [*Hoekstra and Delaney*, 1974]. When the soil temperature rises above −1°C, the thin films of adsorbed water thicken appreciably and increase both the soil's conductivity and the radar wave attenuation coefficient [*Hoekstra and Delaney*, 1974; *Arcone and Delaney*, 1989; *Heggy et al.*, 2001; *Arcone et al.*, 2002]. Figure 5 presents the average temperature as a function of depth in the Fairbanks area for March 2008, as measured by geothermal probes (K. Yoshikawa, personal communication, 2010). We observe that even if the mean surface temperature is −4.7°C, the mean annual temperature of the underlying permafrost is warmer at ~−0.8°C. We therefore assume that, at the Vault Creek site, the soil temperature rises above −1°C at a depth of ~2 m (Figure 4). The increase in dielectric permittivity associated with this increase in temperature is well detected with the GPR at ~30 ns (indicated by the dotted lines in Figures 4b, 4c, and 4d) and likely corresponds to the bottom of the active layer.

Table 1. Dielectric Permittivity of the Fairbanks Silts at 100 MHz (~55%–65% of Water Volumetric Content) for Temperature Below −2°C and Above −1°C[a]

Permittivity	T < -2°C	T > -1°C
ε'	7.3	11
ε''	0.16	0.6

[a] ε' and ε'' are the real and imaginary parts, respectively, of the permittivity [*Arcone and Delaney*, 1984; *Delaney and Arcone*, 1984; *Arcone and Delaney*, 1989].

[31] In order to quantify the different loss mechanisms, the frequency dependency of the dielectric permittivity needs to be understood. Hence, we computed the real and imaginary parts of the dielectric permittivity for each sounding frequency band using the Jonscher law (equation (5)). We set the reference frequency in equation (5) at 100 MHz because the input parameters that we used for applying this equation were measured at this frequency. The Fairbanks silt dielectric permittivity was computed for temperatures below −2°C

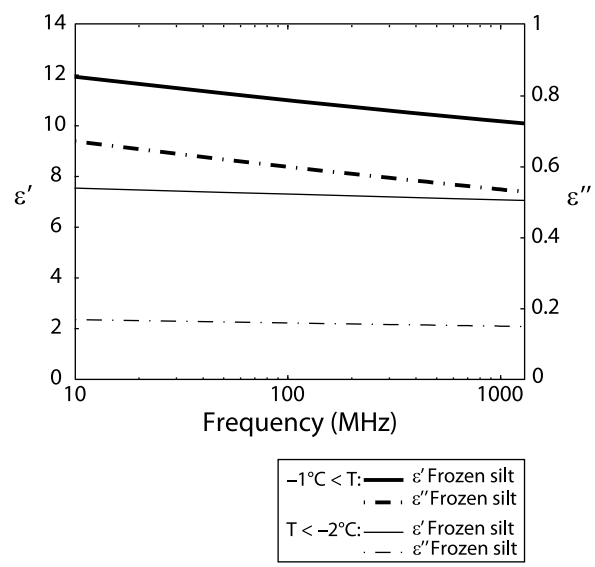

Figure 6. Frequency dependence of the real and imaginary parts of the dielectric constant (computed applying the simplified Jonscher model) [*Hollender and Tillard*, 1998]. The bold lines are the dielectric properties of the Fairbanks frozen silt at $T > -1$°C (below ~2 m), and the thin lines are those of the upper 1.7 m (Fairbanks frozen silt, $T < -2$°C, upper 1.7 m). The solid lines represent the real parts (y axis on the left) and the dash-dotted lines are the imaginary parts (y axis on the right). Permittivity values at the reference frequency 100 MHz (see Table 1) are from the works by *Arcone and Delaney* [1984], *Delaney and Arcone* [1984], and *Arcone and Delaney* [1989].

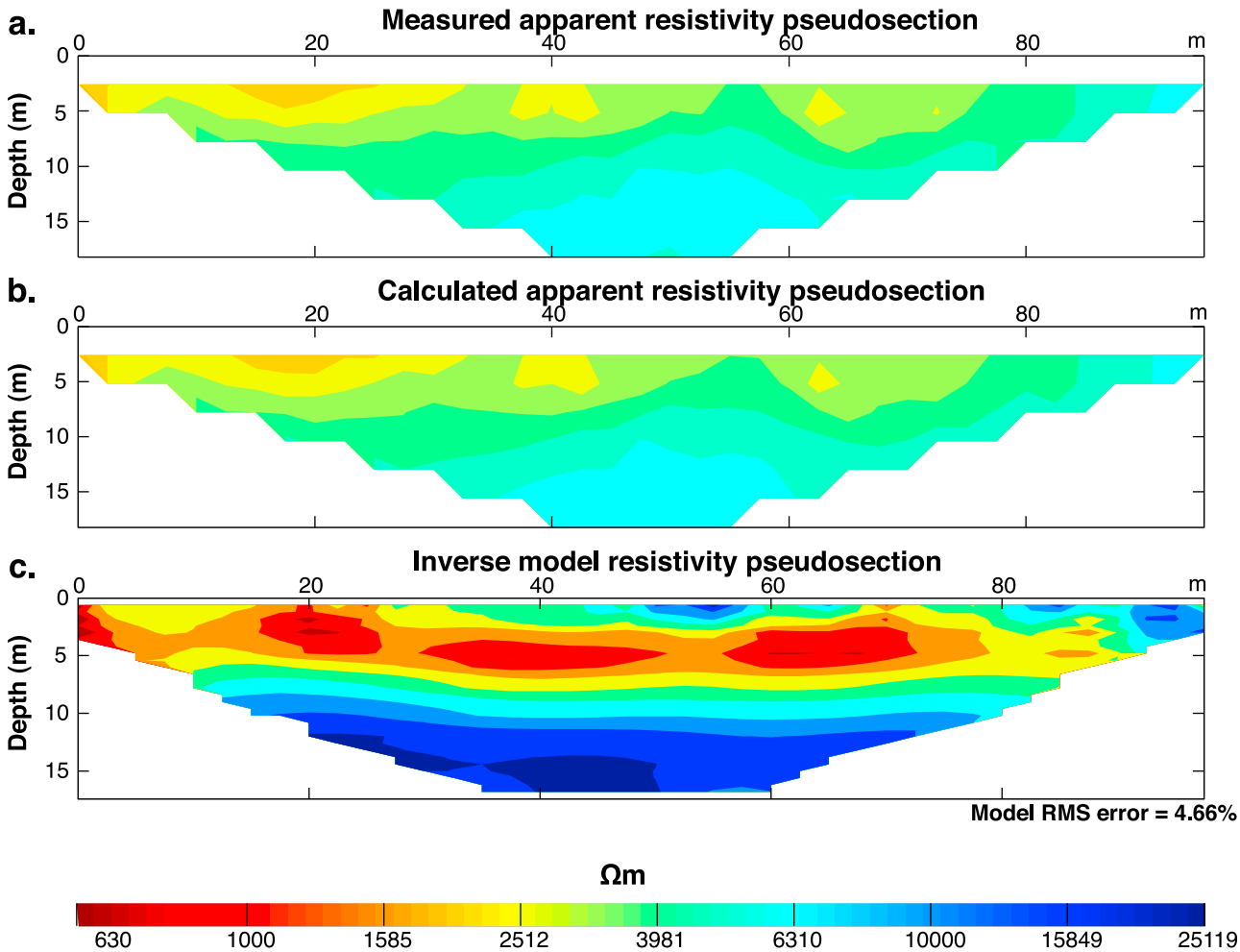

Figure 7. (a) Measured and (b) calculated apparent resistivity pseudosections of the Vault Creek site Wenner ERT survey. (c) The bottom pseudosection is the result of a least squares inversion of the ERT data after eight iterations (RMS error of 4.66%).

and above −1°C. Table 1 presents dielectric permittivities at 100 MHz and for a volumetric water content of ~55% to ~65% [*Arcone and Delaney*, 1984; *Delaney and Arcone*, 1984; *Arcone and Delaney*, 1989]; the Table 1 values are used herein as input parameters when applying the Jonscher law.

[32] Figure 6 shows the frequency dependence of the dielectric permittivity for both the real and imaginary parts, for the Fairbanks silt at $T > -1$°C and $T < -2$°C, which we computed using the Jonscher formulation (cf. equation (5)). For $T < -2$°C (from the surface to ~1.5 m deep), the real part ε' varies from ~7.5 at 10 MHz to ~7 at 1300 MHz, whereas the imaginary part ε'' varies from ~0.17 to 0.15. Thus, ε' and ε'' at T < −2°C do not significantly vary with frequency. However, the dielectric permittivity of the Fairbanks silt for $T > -1$°C (below 2 m deep) decreases with increasing frequency, with ε' and ε'' decreasing from ~11.9 and 0.67, respectively, at 10 MHz to less than 10.1 and 0.53 at 1300 MHz.

4.3. Scattering Loss

[33] Loss in the radar signal also occurs when waves scatter from local interfaces between materials having different dielectric properties. Loss can be severe when size compares with the in situ radar wavelength. The attenuation that is due to scattering can be calculated by subtracting geometric spreading (see section 4.1.) and dielectric attenuation loss (see section 4.2.) from the calculated total signal loss [*Heggy et al.*, 2006a].

5. Survey Results and Discussions

[34] In this section, we present the results from our analysis of the data acquired by the ERT survey (described in section 5.1) and the GPR surveys (section 5.2). Both data sets have an SNR to support the loss separation analysis described above.

5.1. Electrical Resistivity Tomography

[35] The ERT method requires sufficient contact between the ground and the current injection electrodes. During our survey, the contact between electrodes and the frozen ground was constrained by the cold weather conditions (−5°C). Thus, even after six measurement cycles, the standard deviation of some values exceeded 1% (see section 3.1.). We removed eight data points (from a total of 84 measurements) for which the standard deviation of the six measurement cycles exceeded 2%. The measured resistivity data (Figure 7a)

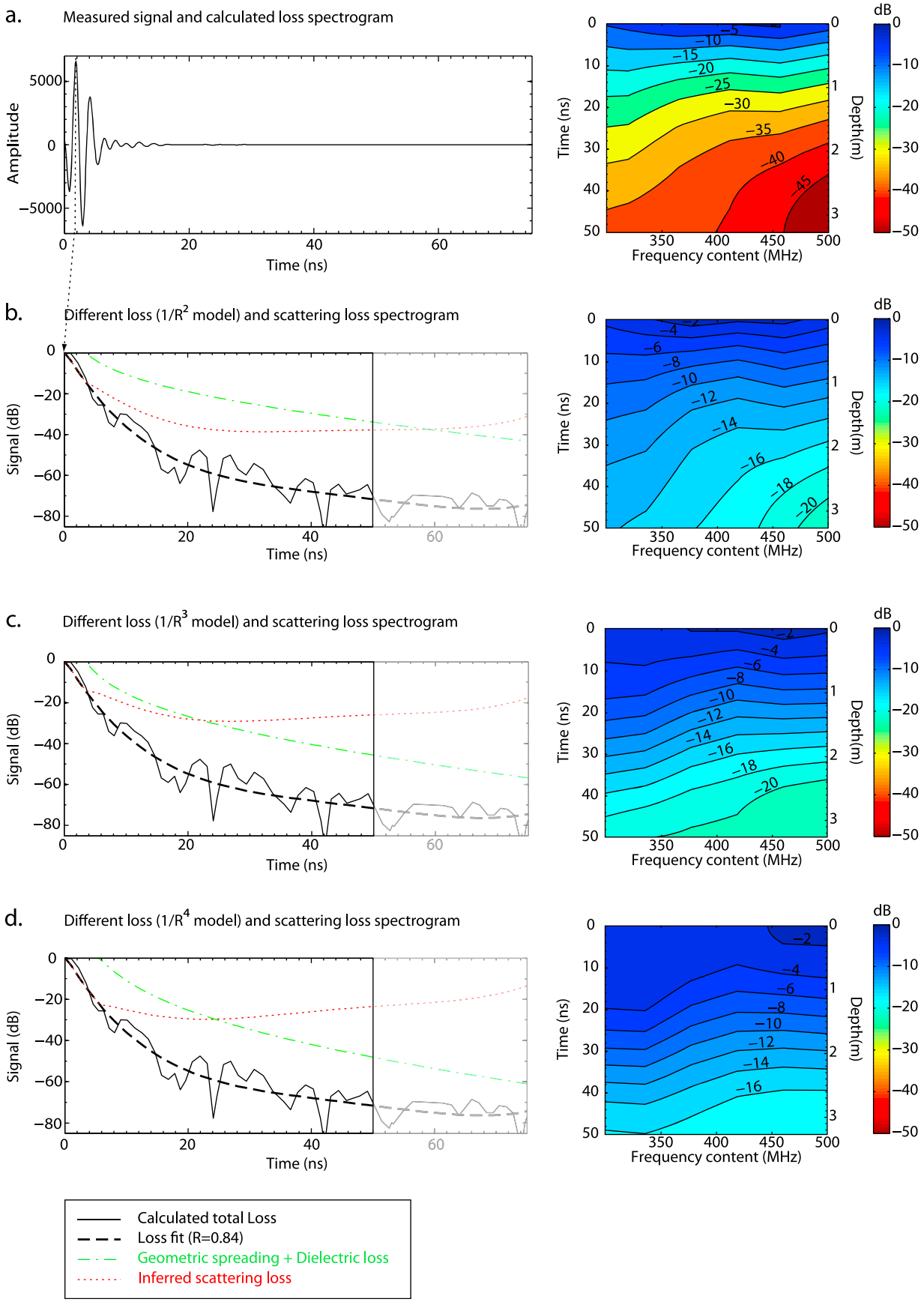
a.
Measured signal and calculated loss spectrogram
Amplitude
Time (ns)
Time (ns)
Depth(m)
Frequency content (MHz)
dB
b.
Different loss (1/R2 model) and scattering loss spectrogram
Signal (dB)
c.
Different loss (1/R3 model) and scattering loss spectrogram
d.
Different loss (1/R4 model) and scattering loss spectrogram
Calculated total Loss
Loss fit (R=0.84)
Geometric spreading + Dielectric loss
Inferred scattering loss

Figure 8

were processed using a finite difference forward modeling package to calculate the apparent resistivity cross section (Figure 7b). A quasi-Newton method was then used to perform a nonlinear least squares inversion [*deGroot-Hedlin and Constable*, 1990; *Loke and Barker*, 1996] to determine geoelectric structure. We used an inverse model composed of 296 blocks, yielding a root-mean-square (RMS) error of <5% after eight iterations (Figure 7c).

[36] The contrast between the near-surface frozen silt and the deeper warmer permafrost cannot be observed because the first 2 m of the ground are not resolvable with the 5 m electrode spacing we used. The inverse resistivity model (Figure 7c) shows low-resistivity lenses (600 to 1000 Ω m) between 2 and 7 m deep. Indeed, even though the silt layer is frozen, the combination of its small grain size (~10 to 100 μm [*Péwé*, 1955], the large specific surface area [*Arcone et al.*, 2008]) and the warmer (>−1°C) temperatures at greater depth (>2 m) yield an increase in the amount of localized unfrozen adsorbed water that causes the local resistivity to decrease with depth over the 2 to 7 m (see section 4.2.). Those low-resistivity values agree with values presented in a previous study on the thermal behavior of the Fairbanks silt resistivity [*Hoekstra et al.*, 1975]. Indeed, the resistivity of the Fairbanks silt (with varying organic content) at −0.7°C measured by *Hoekstra et al.* [1975] varies from 600 to 2000 Ω m.

[37] For depths between 7 and 10 m, Figure 7c shows a progressive increase in resistivity from 3000 to 15,000 Ω m that can be explained by the transition from silt to gravel, observed at a depth of ~10 m in the tunnel (Figure 2). Indeed, the volumetric water content of the gravel layer may be the same as that of the clay-rich silt, but because of the larger grain size, the gravel has a much smaller specific surface area. This, in turn, reduces the gravel's volumetric content of adsorbed water, decreases ion mobility, and increases the gravel layer's resistivity. The location of this transition between the silt and deeper gravel is not well resolved by the inversion because of insufficient vertical resolution of the Wenner configuration, contrary to the case for the horizontal resolution.

[38] In the first 5 m, the average resistivity is ~1200 Ω m (excluding the small, localized low-resistivity lenses). Such high-resistivity values and their associated dielectric attenuation cannot account for all the calculated total loss in the GPR data (see section 5.2). Therefore, ERT survey data analysis allows us to confirm that the calculated total loss in the GPR data is not generated only by the dielectric properties of the subsurface, as discussed below.

5.2. Ground-Penetrating Radar Results

[39] The GPR data processing we used to study the frequency dependence of the different loss mechanisms is relatively different than what we used to visualize the radargrams in Figure 4 because gains were not used for the attenuation analysis. The first step was to remove the gain function that was applied during the field acquisition. We then removed the coherent noise, except for the data acquired with the 40 MHz antenna, with an average-trace-removal filter. Then, we migrated to remove hyperbolas generated by local scatterers in the subsurface. Finally, to improve the SNR and remove the incoherent noise, we calculated the average trace (using the stacking method) over all traces of each GPR profile (74, 227, 228, and 246 traces for the 40, 270, 400, and 900 MHz antenna profiles, respectively); we call this the "amplitude-average trace." Our signal-loss frequency-dependence analysis is hence based on four amplitude-average traces corresponding to the four GPR profiles. For each amplitude-average trace, the signal amplitude was converted into decibels considering the absolute value of the amplitude, at a given time, normalized to the first surface-echo amplitude to eliminate both surface coupling effects and any instrument or antenna interference noise. As the energy information is contained only in the peaks, the total calculated loss curve is computed considering only the local maxima (which correspond to the peaks) of the loss. After having computed the total loss for each trace, we calculated loss generated by the geometric spreading and by the dielectric properties of the medium. Considering the shifted central frequencies of the four GPR surveys (see section 3.2), we applied the radar equation (equation (2)) for the three reflecting target models (smooth or rough planar reflectors and Rayleigh scatterers; see section 4.1). Then, to characterize the frequency behavior of the different signal-loss mechanisms, we computed spectrograms of the total calculated signal loss and those of the scattering loss (for the three models of reflecting target). These were constructed using a Gaussian window width of 97, 22, 22, and 18 ns for the radar data acquired at 40, 270, 400, and 900 MHz, respectively (based on the apodization method). The overlap between consecutive windows is 96.02, 21.2, 21.2, and 17.25 ns. The frequency band of each spectrogram corresponds to the 3 dB frequency bandwidth of the given antenna.

[40] Figure 8 summarizes the analysis for the amplitude-average trace corresponding to the 400 MHz antenna GPR profile. Figure 8a (left) presents the amplitude-average trace as a function of time and Figure 8a (right) shows the corresponding total calculated loss spectrogram. Figures 8b (left)–8d (left) present the different loss signal curves, and Figures 8b (right)–8d (right) show the corresponding residual loss spectrogram. Figures 8b, 8c, and 8d correspond to the loss analyses considering three target models for the radar equation (see section 4.1, equation (2)). The black lines (Figures 8b (left)–8d (left)) are the total calculated loss

Figure 8. Frequency-dependence analysis of the amplitude-average trace of the 400 MHz antenna profile (Figure 4c). (a) (left) Amplitude-average trace versus time (in nanoseconds); (right) corresponding total signal loss spectrogram (in decibels). (left) Graphs of the different loss contributions to the total signal attenuation for (b) the smooth planar interface target model ($1/R^2$), (c) the rough planar interface target model ($1/R^3$), or (d) the Rayleigh scatterer model ($1/R^4$) and (right) their corresponding inferred scattering signal-loss spectrograms. The black dashed lines on the graphs (Figure 8, left) are the polynomial fit (degree 2) of the total signal curve (black thin lines). R is the correlation coefficient. The green dashed lines are the sum of the signal loss generated by the geometric spreading (see equation (2)) and the dielectric attenuation (see equation (4)). The red dashed lines are the inferred scattering loss obtained by removing the geometric spreading and dielectric loss (green dashed lines) to the calculated total loss (thick black dashed lines).

(considering only the peaks), and the black dashed lines are their polynomial fits. The radar effective dynamic range is about 70 dB. The green dashed-dotted lines represent the theoretical loss generated by geometric spreading and dielectric attenuation computed from the radar equation (equations (2) and (4)). The red dotted lines represent the total calculated loss signal after removing the theoretical loss. In the absence of other attenuation mechanisms, we assume that the excess attenuation was generated by scattering. The black frames correspond to the maximum time (or depth) of the spectrograms. The comparison of the three graphs (Figures 8b (left)–8d (left)) shows that the attenuation that is due to geometric spreading is more important for the Rayleigh scatterers model ($1/R^4$ dependency, Figure 8d) than for the smooth plane-interface target model ($1/R^2$ dependency, Figure 8b). Indeed, the theoretical geometric spreading and dielectric loss reach ~60 dB for the $1/R^4$ model compared with ~40 dB for the $1/R^2$ model.

[41] The spectrograms of Figures 8b (right)–8d (right) show that scattering loss decreases as frequency decreases, which we explain by the fact that heterogeneities generate energy loss at wavelengths close to the heterogeneities dimensions. As small scatterers are more numerous than big ones, the scattering phenomenon acts as a low-pass filter, attenuating the higher frequency.

[42] We performed an analysis, shown in Figure 8, for each of the four amplitude-average traces corresponding to the four GPR profiles. To summarize, we deduced from the spectrograms the loss rates (slope) at 3 m for each frequency (at 2 m for the 900 MHz antenna survey data). Figure 9 presents the different loss rates as functions of frequency (calculated total loss rate, deduced dielectric loss rate, and scattering loss rates). These three curves clearly show a relationship of increased loss at higher frequency. Calculated total loss rates (Figure 9, black dots) and scattering loss rates (Figure 9, red crosses) were obtained by calculating the loss rate at 3 m depth at each frequency from the spectrogram of total loss (Figure 8a, right) and the spectrogram of scattering loss (Figures 8b (right)–8d (right)). As mentioned in section 4.1, we consider three types of targets to apply to the radar equation (equation (2)). Thus, the scattering loss rates shown in Figure 9 (red crosses) represent the mean rates deduced from the scattering spectrograms for each reflecting target model (Figures 8b–8d). However, to consider these different models, the error bars of the scattering loss rates (Figure 9, red error bars) account for the standard deviation of the three loss rate values.

[43] Dielectric loss rates (Figure 9, blue circles) were computed at each frequency using the imaginary and real parts of the dielectric constant inferred from the simplified Jonscher law (see equation (5) and Figure 6) as input parameters to equation (4) (see section 4.2). Figure 9 shows a threshold frequency at ~650 MHz where the scattering loss rate (red crosses, Figure 9) and dielectric loss rate (blue circles, Figure 9) are of equal magnitudes. Indeed, the higher the frequency, the higher the dielectric attenuation coefficient (i.e., α: see equation (4)). Quantitatively, the scattering loss rate increases from 0.94 ± 0.37 dB/m at 20 MHz to 9.9 ± 2.35 dB/m at 1000 MHz. The dielectric loss rates at these same frequencies are 0.25 ± 0.03 dB/m and 11.47 ± 1.15 dB/m, respectively. Thus, Figure 9 shows that even at frequencies as low as 20 MHz, the scattering loss rate cannot be neglected. Scattering loss represented between ~45% and 69% (at 1GHz and 20 MHz, respectively) of the total loss rate of a plane wave (i.e., no geometrical spreading), as was the case for both MARSIS and SHARAD.

6. Implication for Ice Identification in Martian Midlatitude Terrains

[44] Although mean annual temperatures at Martian equatorial and midlatitudes average ~50 to 70 K less than in cold-climate terrestrial environments, the apparent presence of potent freezing-point-depressing salts, such as sodium chloride, calcium chloride, and magnesium perchlorate [*Brass*, 1980; *Clark and Van Hart*, 1981; *Burt and Knauth*, 2002; *Hecht et al.*, 2009], suggest that films of adsorbed water could remain unfrozen [*Pommerol et al.*, 2009; *Stillman et al.*, 2010]. Hence, despite an important surface-temperature difference between our study site and the Martian midlatitude to high latitude, the radar propagation characteristics of these two environments may be quite similar because of the presence of adsorbed water. Considering only the dielectric attenuation, the results presented in Figure 6 indicate that ice-rich permafrost can result in higher-than-expected dielectric loss. This is explained by the presence of adsorbed water on mineral grain surfaces, conditions that also appear likely in the salt-rich subsurface of Mars because salts depress freezing points. The study by *Stillman and Grimm* [2011] concerning the different attenuation mechanisms that occur on the SHARAD signal shows that the presence of calcium chloride (concentration >1 M) increases the attenuation rate of SHARAD signal by 33% (at 208 K). Thus, we expect that Martian permafrost in these regions may produce higher absorption for the radar signal than expected if salts are not considered. In this study [*Stillman and Grimm*, 2011], the maximum attenuation rate of 0.27 dB/m that experienced the SHARAD signal is reached for a smectite and fine-grain sand mixture with a specific surface area of 57.6 mg^{-1} (14% by volume smectite) and three monolayers of adsorbed water (without calcium chloride). The dielectric loss rate computed for the Fairbanks silts at 20 MHz (blue circles, Figure 9) is consistent with this result (0.25 ± 0.03 dB/m). Nevertheless, if the three monolayers of adsorbed water present a concentration of calcium chloride >1 M, *Stillman and Grimm* [2011] show that only 9.6% by volume smectite (~38 m^2 g^{-1}) is needed to reach the SHARAD maximum attenuation rate.

[45] Our GPR investigation of the Mars analog environment at Vault Creek suggests that even at low frequencies (10–100 MHz), radar signal loss that is due to volume scattering cannot be neglected. We found that at frequencies below ~650 MHz, the scattering loss rate is higher than the dielectric one, although above this value, the relative strengths of these loss mechanisms are reversed. Based on previous GPR surveys of other Mars analog environments [*Grimm et al.*, 2006; *Heggy et al.*, 2006a], scattering loss values highly depend on the local structure and composition of the subsurface. Indeed, at one volcanic environment (tephra layer of a volcanic cone) investigated at Craters of the Moon National Monument and Preserve (Idaho), *Heggy et al.* [2006a] found that at 16 MHz, the dielectric loss rate exceeded the loss rate that was due to scattering. Conversely, GPR investigations on another volcanic environment,

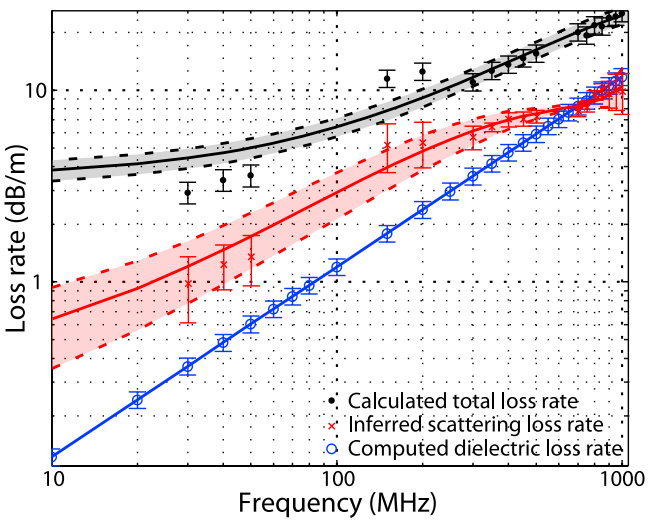

Figure 9. Total, dielectric, and scattering loss rates at 3 m deep (in decibels per meter) as functions of frequency (in megahertz). Black dots are the calculated total loss rates. Red crosses are inferred scattering loss rates. Blue circles are computed dielectric loss rates. Black and red lines are the polynomial fits of the calculated total loss rates and of the inferred scattering loss rates, respectively (extrapolated down to 10 MHz). Black and red transparent areas are delimited by the polynomial fits of the calculated total loss rates and the inferred scattering loss rates, respectively, taking into account the error bars.

conducted by *Grimm et al.* [2006] in the Bishop Tuff volcanic plateau (California), showed that at frequencies of 25 and 50 MHz radar attenuation rates that were due to scattering exceeded those that were due to dielectric loss.

[46] *Heggy et al.* [2006a] suggested that scattering losses of the radar signal across tephras (Inferno Cone) at 20 MHz represent 37% of the total loss, whereas scattering losses measured by the radar signal across the Vault Creek permafrost (this current study) represent ~69% of the radar echo at 20 MHz. Those results are important for the interpretation of the Martian radar sounder data. The loss rate measured by SHARAD over LDAs in Deuteronilus Mensae by *Plaut et al.* [2009] and over the Vastitas Borealis Formation in Amazonis Planitia by *Campbell et al.* [2008] has been assumed to be driven only by dielectric attenuation, neglecting the scattering phenomena generated by the heterogeneity. This is a questionable assumption because the Martian subsurface cannot be considered homogeneous, even at the MARSIS–SHARAD wavelength scale because of the highly fractured megaregolith.

[47] As mentioned in section 2.2, the Vault Creek site can be considered a reasonable analog to the Deuteronilus Mensae area. Thus, with our scattering loss quantified, we now constrain the imaginary part of the dielectric permittivity, which we inferred from the dielectric attenuation after subtracting the scattering loss, to identify the ice signature as measured by *Plaut et al.* [2009]. In this section, we also consider the loss rate measured by SHARAD over the Vastitas Borealis Formation [*Campbell et al.*, 2008]. As this Martian region is known to have a volcanic origin [*Tanaka et al.*, 2005], we consider the scattering loss values inferred from the *Heggy et al.* [2006a] study over a volcanic terrain. The estimate of the dielectric attenuation after removing the scattering component provides a more accurate estimate of the imaginary part of the dielectric permittivity. This, in turn, will allow us to constrain the ambiguity on the compositions of Deuteronilus Mensae and Amazonis Planitia. Table 2 presents the revised dielectric loss rate in decibels per meter after removing the scattering component. We considered two models for scattering loss (volcanic subsurface for Vastitas Borealis Formation in Amazonis and ice-rich subsurface for LDAs in Deuteronilus) accounting for 37% [*Heggy et al.*, 2006a] and 69% (this study) of the total signal for a real part of a dielectric constant of 3. Deduced imaginary parts of the permittivity are 0.004 in the region of Deuteronilus Mensae and ranged from 0.011 to 0.018 for Amazonis Planitia.

[48] For Deuteronilus Mensae, the above value agrees with the range of those inferred from lab measurements for an ice and tephra powder mixture ($\varepsilon'' \sim 0.006$–0.015) [*Phillips et al.*, 2008, supporting online material] for a dielectric constant of 3. Those results suggest that the ice deposit detected by SHARAD over the LDAs in Deuteronilus Mensae is more ice rich than originally believed. LDAs have been hypothesized to be residues of a much larger glacier protected from sublimation by a thin layer of debris [*Head et al.*, 2005, 2006; *Marchant and Head*, 2007;

Table 2. Revised Two-Way Dielectric Attenuation Coefficient Calculated From SHARAD Data Over Deuteronilus Mensae [*Plaut et al.*, 2009] and Amazonis Planitia [*Campbell et al.*, 2008] Applying 69% (This Study) and 37% [*Heggy et al.*, 2006a], Respectively, of Scattering Loss for a Permittivity Real Part (Dielectric Constant) of 3[a]

	For $\varepsilon' = 3$					
	Calculated Loss Rate Not Considering Scattering		Considering 37% Scattering Loss, Volcanic Subsurface		Considering 69% Scattering Loss, Ice-Rich Subsurface	
	α_{tot}(dB/m)	ε^2	α_{diel}(dB/m)	ε^2	α_{diel}(dB/m)	ε^2
Deuteronilus Mensae	0.026[b]	0.012	-	-	0.008	0.004
	0.061[c]	0.029	0.038	0.018	-	-
Amazonis Planitia	0.036[c]	0.017	0.023	0.011	-	-
	0.058[c]	0.028	0.037	0.017	-	-
	0.060[c]	0.029	0.038	0.018	-	-

[a]The quantities α_{tot}, α_{diel}, and ε'' are the total calculated attenuation coefficient, the revised dielectric attenuation coefficient, and the imaginary part of the permittivity, respectively.
[b]From *Plaut et al.* [2009].
[c]From *Campbell et al.* [2008].

Plaut et al., 2009]. Our result agrees with this hypothesis, which implies that the ice content in the LDAs is significant. It could thus correspond to the hypothesis of debris-covered glaciers covered by a thin debris lag in which the amount of ice could be higher than 80% [*Head et al.*, 2005, 2006].

[49] For Amazonis Planitia, the imaginary parts of the permittivity values are too high to represent an ice-rich terrain (except for one SHARAD profile). Thus, these imaginary parts of the material comprising the Vastitas Borealis Formation in Amazonis Planitia are a closer match to the one measured in volcanic resistive terrains such as low-loss basaltic lava flows or ashes mixed with a small amount of ice. As Amazonis Planitia is located west of Olympus Mons volcano, this area has been interpreted to be a volcanic sedimentary basin [*Fuller and Head*, 2002; *Tanaka et al.*, 2005]. Our result is consistent with this interpretation, with a possible small amount of ice in a basaltic rock matrix.

[50] These results should be considered with caution, as radar signal loss from volume scattering varies with the degree and scale of subsurface heterogeneity. The Martian subsurface may exhibit far greater heterogeneity than the temperate permafrost environment of interior Alaska and the volcanic environment of inferno cones (Idaho) because of the cratering that generates the megaregolith and important volcanism. This, in turn, may create heterogeneities that are especially apparent at the lower frequencies employed by MARSIS and SHARAD. As mentioned in section 2.1, permafrost on Earth can exhibit high heterogeneity because of the formation of ice structures like ice wedges or segregation lenses. This is also likely the case for the midlatitude to high-latitude ice-rich terrains on Mars. Thus, we consider that the scattering loss rate deduced in this work (69% at 20 MHz) and in the study by *Heggy et al.* [2006a] (37% at 20 MHz) could be seen as the range end values of the loss rate generated by scattering phenomena that can be encountered in the Martian upper frozen regolith at the SHARAD frequency.

[51] Loss rate values presented herein at higher frequencies (400 and 900 MHz antenna surveys) are relevant to the potential signal loss that can be encountered by future GPR experiments planned to probe the Martian shallow subsurface (e.g., WISDOM GPR experiment planned for the ExoMars rover mission [*Ciarletti et al.*, 2009]).

[52] To further constrain the range of loss likely to be encountered by the MARSIS, SHARAD, and WISDOM GPRs will require the investigation of a considerably broader range of terrestrial analogs, an effort that we continue to pursue. GPR investigations of Mars analog environments should survey as wide a range of this characteristic as they do of comparable variations in analog lithology and composition.

[53] **Acknowledgments.** We express our gratitude to Lucie Rolland and Fernand Lopes from IPGP for the helpful discussions and comments. This work was supported in part by NASA Mars Fundamental Research grant NNG05GL39G and by the NASA Planetary Geology and Geophysics Program grant PGG04-000-0059. Additional support was provided by Centre National d'Etudes Spatiales (CNES) and by a French Ministry of Research and Technology Ph.D. grant for Boisson. We are grateful to Steven A. Arcone and an anonymous reviewer whose comments and suggestions were of great assistance in the revision of the manuscript. Part of this research was carried out at the Jet Propulsion Laboratory, California Institute of Technology, under a contract with the National Aeronautics and Space Administration. This is IPGP contribution number 3212 and LPI contribution number 1561.

References

Anderson, D. M., and A. R. Tice (1973), The unfrozen interfacial phase in frozen soil water systems, in *Ecological Studies. Analysis and Synthesis*, vol. 4, edited by A. Hadas et al., pp. 107–124, Springer, New York.

Anderson, D. M., E. S. Gaffney, and P. F. Low (1967), Frost phenomena on Mars, *Science*, *155*, 319–322, doi:10.1126/science.155.3760.319.

Annan, A. P., and J. L. Davis (1977), Radar range analysis for geological materials, *Pap. Geol. Surv. Can.*, *77–1B*, 117–124.

Arcone, S. A. (1984), Pulse transmission through frozen silt, *CRREL Rep. 84-17*, U.S. Army Cold Reg. Res. and Eng. Lab., Hanover, N. H.

Arcone, S. A., and A. J. Delaney (1984), Field dielectric measurements of frozen silt using VHF pulses, *Cold Reg. Sci. Technol.*, *9*, 29–37, doi:10.1016/0165-232X(84)90045-4.

Arcone, S. A., and A. J. Delaney (1989), Investigations of dielectric properties of some frozen materials using cross-borehole radiowave pulse transmission, *CRREL Rep. 89-4*, 18 pp., U.S. Army Cold Reg. Res. and Eng. Lab., Hanover, N. H.

Arcone, S. A., and A. J. Delaney (2003), Radiowave pulse refraction and ground wave propagation through permafrost and the active layer, in *Permafrost, Proc. Int. Conf. Permafrost, 8th*, pp. 21–26, A. A. Balkema, Lisse, Netherlands.

Arcone, S. A., M. L. Prentice, and A. J. Delaney (2002), Stratigraphic profiling with ground-penetrating radar in permafrost: A review of possible analogs for Mars, *J. Geophys. Res.*, *107*(E11), 5108, doi:10.1029/2002JE001906.

Arcone, S. A., S. Grant, G. Boitnott, and B. Bostick (2008), Complex permittivity and clay mineralogy of grain-size fractions in a wet silt soil, *Geophysics*, *73*(3), 1–13, doi:10.1190/1.2890776.

Ballou, E. V., P. C. Wood, T. Wydeven, M. E. Lehwalt, and R. E. Mack (1978), Chemical interpretation of Viking Lander 1 life detection experiment, *Nature*, *271*, 644–645, doi:10;1038/271644a0.

Banin, A., and D. M. Anderson (1974), Effects of salt concentration changes during freezing on the unfrozen water content of porous materials, *Water Resour. Res.*, *10*, 124–128, doi:10.1029/WR010i001p00124.

Bano, M. (1996), Constant dielectric losses of ground penetrating radar-waves, *Geophys. J. Int.*, *124*, 279–288, doi:10.1111/j.1365-246X.1996.tb06370.x.

Bibring, J.-P., et al. (2006), Mars surface diversity as revealed by the OMEGA/Mars Express observations, *Science*, *307*, 1576–1581, doi:101126/science.1108806.

Boike, J., and K. Yoshikawa (2003), Mapping of periglacial geomorphology using kite/balloon aerial photography, *Permafrost Periglacial Process.*, *14*(1), 18–85, doi:10.1002/ppp.437.

Brass, G. W. (1980), Stability of brines on Mars, *Icarus*, *42*, 20–28, doi:10.1016/0019-1035(80)90237-7.

Burr, D. M., K. L. Tanaka, and K. Yoshikawa (2009), Pingos on Earth and Mars, *Icarus*, *57*, 541–555.

Burt, D., and L. P. Knauth (2002), Electrically conducting, Ca-rich brines, rather than water, expected in the Martian subsurface, *J. Geophys. Res.*, *108*(E4), 8026, doi:10.1029/2002JE001862.

Campbell, B., L. Carter, R. Phillips, J. Plaut, N. Putzig, A. Safaeinili, R. Seu, D. Biccari, A. Egan, and R. Orosei (2008), SHARAD radar sounding of the Vastitas Borealis Formation in Amazonis Planitia, *J. Geophys. Res.*, *113*, E12010, doi:10.1029/2008JE003177.

Carr, M. H. (1986), Mars: A water-rich planet?, *Icarus*, *68*, 187–216, doi:10.1016/0019-1035(86)90019-9.

Carr, M. H. (1996), *Water on Mars*, Oxford Univ. Press, New York.

Carr, M. H., and G. G. Schaber (1977), Martian permafrost features, *J. Geophys. Res.*, *82*(28), 4039–4054, doi:10.1029/JS082i028p04039.

Carter, L. M., et al. (2009), Shallow radar (SHARAD) sounding observations of the Medusae Fossae Formation, Mars, *Icarus*, *199*(2), 295–302, doi:10.1016/j.icarus.2008.10.007.

Ciarletti, V., C. Corbel, F. Cais, D. Plettemeier, S. E. Hamran, M. Øyan, and the WISDOM team (2009), Performances of the WISDOM GPR designed for the shallow sounding of Mars, *Lunar Planet. Sci.*, *XL*, Abstract 2367.

Clark, B. C., and D. C. Van Hart (1981), The salts of Mars, *Icarus*, *45*, 370–378, doi:10.1016/0019-1035(81)90041-5.

Clifford, S. M. (1993), A model for the hydrologic and climatic behavior of water on Mars, *J. Geophys. Res.*, *98*, 10,973–11,016, doi:10.1029/93JE00225.

Clifford, S. M., and T. J. Parker (2001), The evolution of the Martian hydrosphere: Implications for the fate of a primordial ocean and the cur-

rent state of the Northern Plains, *Icarus*, *154*, 40–79, doi:10.1006/icar.2001.6671.
Clifford, S. M., J. Lasue, E. Heggy, J. Boisson, P. McGovern, and M. D. Max (2010), Depth of the Martian cryosphere: Revised estimates and implications for the existence and detection of subpermafrost groundwater, *J. Geophys. Res.*, *115*, E07001, doi:10.1029/2009JE003462.
Costard, F. M., and J. S. Kargel (1995), Outwash plains and thermokarst on Mars, *Icarus*, *114*, 93–112, doi:10.1006/icar.1995.1046.
Costard, F., E. Gautier, and D. Brunstein (2007), Siberian rivers and Martian outflow channels: An analogy, in *The Geology of Mars: Evidence from Earth-Based Analogs*, edited by M. G. Chapman, pp. 279–296, Cambridge Univ. Press, Cambridge, U. K., doi:10.1017/CBO9780511536014.012.
deGroot-Hedlin, C., and S. Constable (1990), Occam's inversion to generate smooth, two-dimensional models form magnetotelluric data, *Geophysics*, *55*, 1613–1624, doi:10.1190/1.1442813.
Delaney, A. J., and S. A. Arcone (1982), Laboratory measurements of soil electric properties between 0.1 and 5 GHz, *CRREL Rep. 82-10*, U.S. Army Cold Reg. Res. and Eng. Lab., Hanover, N. H.
Delaney, A. J., and S. A. Arcone (1984), Dielectric measurements of frozen silt using time domain reflectometry, *Cold Reg. Sci. Technol.*, *9*(1), 39–46, doi:10.1016/0165-232X(84)90046-6.
Dundas, C. M., and A. S. McEwen (2010), An assessment of evidence for pingos on Mars using HiRISE, *Icarus*, *205*, 244–258, doi:10.1016/j.icarus.2009.02.020.
Fairén, A. G., A. F. Davila, L. Gago-Duport, R. Amils, and C. P. McKay (2009), Stability against freezing of aqueous solutions on early Mars, *Nature*, *459*, 401–404, doi:10.1038/nature07978.
Fanale, F. P., J. R. Salvail, A. P. Zent, and S. E. Postawko (1986), Global distribution and migration of subsurface ice on Mars, *Icarus*, *67*, 1–18, doi:10.1016/0019-1035(86)90170-3.
Farr, T. G. (2004), Terrestrial analogs to Mars: The NRC community decadal report, *Planet. Space Sci.*, *52*, 3–10, doi:10.1016/j.pss.2003.08.004.
Farr, T. G., et al. (2001), *NRC Decadal Study of Terrestrial Analogues to Mars*, Natl. Res. Counc, Washington, D.C.
Fuller, E. R., and J. W. Head III (2002), Amazonis Planitia: The role of geologically recent volcanism and sedimentation in the formation of the smoothest plains on Mars, *J. Geophys. Res.*, *107*(E10), 5081, doi:10.1029/2002JE001842.
Grant, J. A., T. A. Maxwell, A. K. Johnston, C. J. Leuschen, A. E. Schutz, and K. K. Williams (2004), Using ground penetrating radar to constrain the drainage evolution in southern Egypt and implications for future deployment on Mars, *Eos Trans. AGU*, *85*(17), Jt. Assem. Suppl., Abstract P53A-04.
Grimm, R. E., and S. L. Painter (2009), On the secular evolution of groundwater on Mars, *Geophys. Res. Lett.*, *36*, L24803, doi:10.1029/2009GL041018.
Grimm, R. E., E. Heggy, S. Clifford, C. Dinwiddie, R. McGinnis, and D. Farrell (2006), Absorption and scattering in ground-penetrating radar: Analysis of the Bishop Tuff, *J. Geophys. Res.*, *111*, E06S02, doi:10.1029/2005JE002619.
Head, J. W., J. F. Mustard, M. A. Kreslavsky, R. E. Milliken, and D. R. Marchant (2003), Recent ice ages on Mars, *Nature*, *426*, 797–802, doi:10.1038/nature02114.
Head, J. W., et al. (2005), Tropical to mid-latitude snow and ice accumulation, flow and glaciation on Mars, *Nature*, *434*, 346–351, doi:10.1038/nature03359.
Head, J. W., D. R. Marchand, M. C. Agnew, C. I. Fassett, and M. A. Kreslavsky (2006), Extensive valley glacier deposits in the northern mid-latitudes of Mars: Evidence for Late Amazonian obliquity-driven climate change, *Earth Planet. Sci. Lett.*, *241*, 663–671, doi:10.1016/j.epsl.2005.11.016.
Hecht, M. H., et al. (2009), Detection of perchlorate and the soluble chemistry of Martian soil at the Phoenix lander site, *Science*, *325*, 64–67.
Heggy, E., P. Paillou, G. Ruffié, J. M. Malézieux, F. Costard, and G. Grandjean (2001), On water detection in the Martian subsurface using sounding radar, *Icarus*, *154*(2), 244–257, doi:10.1006/icar.2001.6717.
Heggy, E., S. M. Clifford, R. E. Grimm, C. L. Dinwiddie, D. Y. Wyrick, and B. E. Hill (2006a), Ground-penetrating radar sounding in mafic lava flows: Assessing attenuation and scattering losses in Mars-analog volcanic terrains, *J. Geophys. Res.*, *111*, E06S04, doi:10.1029/2005JE002589.
Heggy, E., S. M. Clifford, R. E. Grimm, C. L. Dinwiddie, J. A. Stamatakos, and S. H. Gonzalez (2006b), Low-frequency radar sounding investigations of the North Amargosa Desert, Nevada: A potential analog of conductive subsurface environments on Mars, *J. Geophys. Res.*, *111*, E06S03, doi:10.1029/2005JE002523.
Hiesinger, H., and J. W. Head III (2000), Characteristics and origin of polygonal terrain in southern Utopia Planitia, Mars: Results from Mars Orbiter Laser Altimeter and Mars Orbiter Camera data, *J. Geophys. Res.*, *105*(E5), 11,999–12,022, doi:10.1029/1999JE001193.
Hoekstra, P., and A. Delaney (1974), Dielectric properties of soils at UHF and microwave frequencies, *J. Geophys. Res.*, *79*, 11,1699–11,1708.
Hoekstra, P., P. V. Sellmann, and A. Delaney (1975), Ground and airborne resistivity surveys of permafrost near Fairbanks, Alaska, *Geophysics*, *40*(4), 641–656, doi:10.1190/1.1440555.
Hollender, F., and S. Tillard (1998), Modeling ground-penetrating radar wave propagation and reflection with the Jonscher parameterization, *Geophysics*, *63*, 1933–1942, doi:10.1190/1.1444486.
Jonscher, A. K. (1977), The universal dielectric response, *Nature*, *267*, 673–679, doi:10.1038/267673a0.
Kargel, J. S., J. Moore, and T. Parker (1993), Workshop on the Martian Northern Plains, Sedimentological, Periglacial, and Paleoclimatic Evolution, *LPI Tech. Rep. 93–04*, Lunar and Planet. Inst., Houston, Tex.
Kuzmin, R. O. (1983), *Cryolithosphere of Mars*, Nauka, Moscow.
Lefort, A., P. S. Russell, and N. Thomas (2010), Scalloped terrains in the Peneus and Amphitrites Paterae region of Mars as observed by HiRISE, *Icarus*, *205*, 259–268, doi:10.1016/j.icarus.2009.06.005.
Leuschen, C., P. Kanagaratnam, K. Yoshikawa, S. Arcone, and P. Gogineni (2003), Design and field experiments of a ground penetrating radar for Mars exploration, *J. Geophys. Res.*, *108*(E4), 8034, doi:10.1029/2002JE001876.
Levy, J., J. Head, and D. Marchant (2009), Thermal contraction crack polygons on Mars: Classification, distribution, and climate implications from HiRISE observations, *J. Geophys. Res.*, *114*, E01007, doi:10.1029/2008JE003273.
Loke, M. H., and R. D. Barker (1996), Rapid least-squares inversion of apparent resistivity pseudosections by a quasi-Newton method, *Geophys. Prospect.*, *44*, 131–152, doi:10.1111/j.1365-2478.1996.tb00142.x.
Lucchitta, B. K. (1981), Mars and Earth: Comparison of cold-climate features, *Icarus*, *45*, 264–303, doi:10.1016/0019-1035(81)90035-X.
Lucchitta, B. K. (1985), Geomorphic evidence of ground ice on Mars, in Ices in the Solar System, edited by J. Klinger et al., pp. 583–604, Reidel, Hingham, Mass.
Mangold, N. (2003), Geomorphic analysis of lobate debris aprons on Mars at Mars Orbiter Camera scale: Evidence for ice sublimation initiated by fractures, *J. Geophys. Res.*, *108*(E4), 8021, doi:10.1029/2002JE001885.
Mangold, N. (2005), High latitude patterned grounds on Mars: Classification, distribution and climatic control, *Icarus*, *174*, 336–359, doi:10.1016/j.icarus.2004.07.030.
Mangold, N., P. Allemand, P. Thomas, P. Duval, and Y. Géraud (2002), Experimental and theoretical deformation of ice-rock mixtures: Implications on rheology and ice content of Martian permafrost, *Planet. Space Sci.*, *50*, 385–401, doi:10.1016/S0032-0633(02)00005-3.
Mangold, N., S. Maurice, W. C. Feldman, F. Costard, and F. Forget (2004), Spatial relationships between patterned ground and ground ice detected by the Neutron Spectrometer on Mars, *J. Geophys. Res.*, *109*, E08001, doi:10.1029/2004JE002235.
Marchant, D. R., and J. W. Head III (2007), Antarctic dry valleys: Microclimate zonation, variable geomorphic processes, and implications for assessing climate change on Mars, *Icarus*, *192*, 187–222, doi:10.1016/j.icarus.2007.06.018.
Marchenko, S., V. Romanovsky, and G. Tipenko (2008) Numerical modeling of spatial permafrost dynamics in Alaska, in *Proceedings of the Ninth International Conference on Permafrost*, vol. 2, pp. 1125–1130, Univ. of Alaska Press, Fairbanks.
Mellon, M. T., and B. M. Jakosky (1993), Geographic variations in the thermal and diffusive stability of ground ice on Mars, *J. Geophys. Res.*, *98*, 3345–3364, doi:10.1029/92JE02355.
Mellon, M. T., and B. M. Jakosky (1995), The distribution and behavior of Martian ground ice during past and present epochs, *J. Geophys. Res.*, *100*(E6), 11,781–11,799, doi:10.1029/95JE01027.
Mellon, M. T., R. E. Arvidson, J. J. Marlow, R. J. Phillips, and E. Asphaug (2008), Periglacial landforms at the Phoenix landing site and the northern plains of Mars, *J. Geophys. Res.*, *113*, E00A23, doi:10.1029/2007JE003039.
Mouginis-Mark, P. J. (1985), Volcano/ground ice interactions in Elysium Planitia, Mars, *Icarus*, *64*, doi:10.1016/0019-1035(85)90090-9.
Mustard, J. F., et al. (2008), Hydrated silicate minerals on Mars observed by the Mars Reconnaissance Orbiter CRISM instrument, *Nature*, *454*, 305–309, doi:10.1038/nature07097.
Mutch, T. A., et al. (1976), The surface of Mars: The view from the Viking 2 Lander, *Science*, *194*(4271), 1277–1283, doi:10.1126/science.194.4271.1277.
Newberry, R. J., T. K. Bundtzen, K. H. Clautice, R. A. Combellick, T. Douglas, G. M. Laird, S. A. Liss, D. S. Pinney, R. R. Reifenstuhl, and D. N. Solie (1996), Preliminary geologic map of the Fairbanks

mining district, Alaska, *Public Data File 96–16*, scale 1:63360, Alaska Div. of Geol. and Geophys. Surv., Fairbanks, Alaska.

Paillou, P., G. Grandjean, J.-M. Malézieux, G. Ruffié, E. Heggy, D. Piponnier, P. Dubois, and J. Achache (2001), Performances of ground penetrating radars in arid volcanic regions: Consequences for Mars subsurface exploration, *Geophys. Res. Lett.*, *28*(5), 911–914, doi:10.1029/1999GL008449.

Péwé, T. L. (1955), Origin of the upland silt near Fairbanks, Alaska, *Geol. Soc. Am. Bull.*, *66*, 699–724, doi:10.1130/0016-7606(1955)66[699:OOTUSN]2.0.CO;2.

Phillips, R. J., et al. (2008), Mars north polar deposits: Stratigraphy, age, and geodynamical response, *Science*, *320*, 1182–1185, doi:10.1126/science.1157546.

Picardi, G., et al. (2004), Performance and surface scattering models for the Mars Advanced Radar for Subsurface and Ionosphere Sounding (MARSIS), *Planet. Space Sci.*, *52*, 149–156, doi:10.1016/j.pss.2003.08.020.

Plaut, J. J., A. Safaeinili, J. W. Holt, R. J. Phillips, J. W. Head, R. Seu, N. E. Putzig, and A. Frigeri (2009), Radar evidence for ice in lobate debris aprons in the mid-northern latitudes of Mars, *Geophys. Res. Lett.*, *36*, L02203, doi:10.1029/2008GL036379.

Pommerol, A., B. Schmitt, P. Beck, and O. Brissaud (2009), Water sorption on Martian regolith analogs: Thermodynamics and near-infrared reflectance spectroscopy, *Icarus*, *204*, 114–136, doi:10.1016/j.icarus.2009.06.013.

Poulet, F., J.-P. Bibring, J. F. Mustard, A. Gendrin, N. Mangold, Y. Langevin, R. E. Arvidson, B. Gondet, C. Gomez, and the Omega team (2005), Phyllosilicates on Mars and implications for early Martian climate, *Nature*, *438*, 623–627, doi:10.1038/nature04274.

Reynolds, J. M. (1997), *An Introduction to Applied and Environmental Geophysics*, pp. 694–695, John Wiley, Hoboken, N. J.

Rossbacher, L. A., and S. Judson (1981), Ground ice on Mars: Inventory, distribution, and resulting landforms, *Icarus*, *45*, 39–59, doi:10.1016/0019-1035(81)90005-1.

Séjourné, A., F. Costard, J. Gargani, R. J. Soare, A. Fedorov, and C. Marmo (2011), Scalloped depressions and small-sized polygons in western Utopia Planitia, Mars: A new formation hypothesis, *Planet. Space Sci.*, *59*, 412–422, doi:10.1016/j.pss.2011.01.007.

Sellmann, P. V. (1967), Geology of the USA CRREL permafrost tunnel, Fairbanks, Alaska, *CRREL Tech. Rep. 199*, 22 pp., U.S. Army Cold Reg. Res. and Eng. Lab., Hanover, N. H.

Seu, R., D. Biccari, R. Orosei, L. V. Lorenzoni, R. J. Phillips, L. Marinangeli, G. Picardi, A. Masdea, and E. Zampolini (2004), SHARAD: The MRO 2005 shallow radar, *Planet. Space Sci.*, *52*(1–3), 157–166, doi:10.1016/j.pss.2003.08.024.

Skolnik, M. (1990), *Radar Handbook*, 2nd ed., pp. 1, 6, McGraw-Hill, New York.

Smith, P. H., et al. (2007), The Phoenix Mission, paper presented at the 7th International Conference on Mars, Lunar and Planet. Inst., Pasadena, Calif., 9–13 July.

Soare, R. J., J. S. Kargel, G. R. Osinski, and F. Costard (2007), Thermokarst processes and the origin of crater-rim gullies in Utopia and western Elysium Planitia, *Icarus*, *191*(1), 95–112, doi:10.1016/j.icarus.2007.04.018.

Squyres, S. W. (1978), Martian fretted terrain: Flow of erosional debris, *Icarus*, *34*, 600–613, doi:10.1016/0019-1035(78)90048-9.

Squyres, S. W. (1979), The distribution of lobate debris aprons and similar flows on Mars, *J. Geophys. Res.*, *84*, 8087–8096, doi:10.1029/JB084iB14p08087.

Squyres, S. W., and M. H. Carr (1986), Geomorphic evidence for the distribution of ground ice on Mars, *Science*, *231*, 249–252, doi:10.1126/science.231.4735.249.

Squyres, S. W., S. M. Clifford, R. O. Kuzmin, J. R. Zimbelman, and F. M. Costard (1992), Ice in the Martian regolith, in *Mars*, edited by H. H. Kieffer, B. M. Jakosky, C. W. Snyder, and M. S. Matthews, pp. 523–554, Univ. of Arizona Press, Tucson.

Stillman, D. E., and R. E. Grimm (2011), Radar penetrates only the youngest geological units on Mars, *J. Geophys. Res.*, *116*, E03001, doi:10.1029/2010JE003661.

Stillman, D. E., R. E. Grimm, and S. T. Dec (2010), Low-frequency electrical properties of ice-silicate mixture, *J. Phys. Chem. B*, *114*, 6065–6073, doi:10.1021/jp9070778.

Stratton, J. A. (1941), *Electromagnetic Theory*, McGraw-Hill, New York.

Tanaka, K. L., J. A. Skinner, and T. M. Hare (2005), Geologic map of the northern plains of Mars, *U. S. Geol. Surv. Sci. Invest. Map*, *2888*.

Ulaby, F. T., R. K. Moore, and A. K. Fung (1982), Microwave remote sensing: Active and passive, in *Radar Remote Sensing and Surface Scattering and Emission Theory*, *Adv. Book Prog. Ser.*, vol. II, 609 pp., Addison-Wesley, Reading, Mass.

Watters, T. R., et al. (2007), Radar sounding of the Medusae Fossae Formation Mars: Equatorial ice or dry, low-density deposits?, *Science*, *318*(5853), 1125–1128, doi:10.1126/science.1148112.

Yoshikawa, K. (2003), Origin of the polygons and the thickness of Vastitas Borealis Formation in Western Utopia Planitia on Mars, *Geophys. Res. Lett.*, *30*(12), 1603, doi:10.1029/2003GL017165.

Yoshikawa, K., C. Leuschen, A. Ikeda, K. Harada, P. Gogineni, P. Hoekstra, L. Hinzman, Y. Sawada, and N. Matsuoka (2006), Comparison of geophysical investigations for detection of massive ground ice (pingo ice), *J. Geophys. Res.*, *111*, E06S19, doi:10.1029/2005JE002573.

Zent, A. P. (2008), A historical search for habitable ice at the Phoenix landing site, *Icarus*, *196*, 385–408, doi:10.1016/j.icarus.2007.12.028.

A. Anglade, J. Boisson, and P. Lognonné, Institut de Physique du Globe de Paris et Université Paris Diderot, Sorbonne Paris Cité, UMR CNRS 7154, 4 avenue de Neptune, F-94100 Saint Maur des Fossés, France. (boisson@ipgp.jussieu.fr)

S. M. Clifford, Lunar and Planetary Institute, 3600 Bay Area Blvd., Houston, TX 77058, USA.

E. Heggy, Jet Propulsion Laboratory, 4800 Oak Grove Dr., MS 300-243, Pasadena, CA 91109, USA. (heggy@jpl.nasa.gov)

K. Yoshikawa, Water and Environmental Research Center, University of Alaska Fairbanks, PO Box 755860, Fairbanks, AK 99775-55860, USA.